

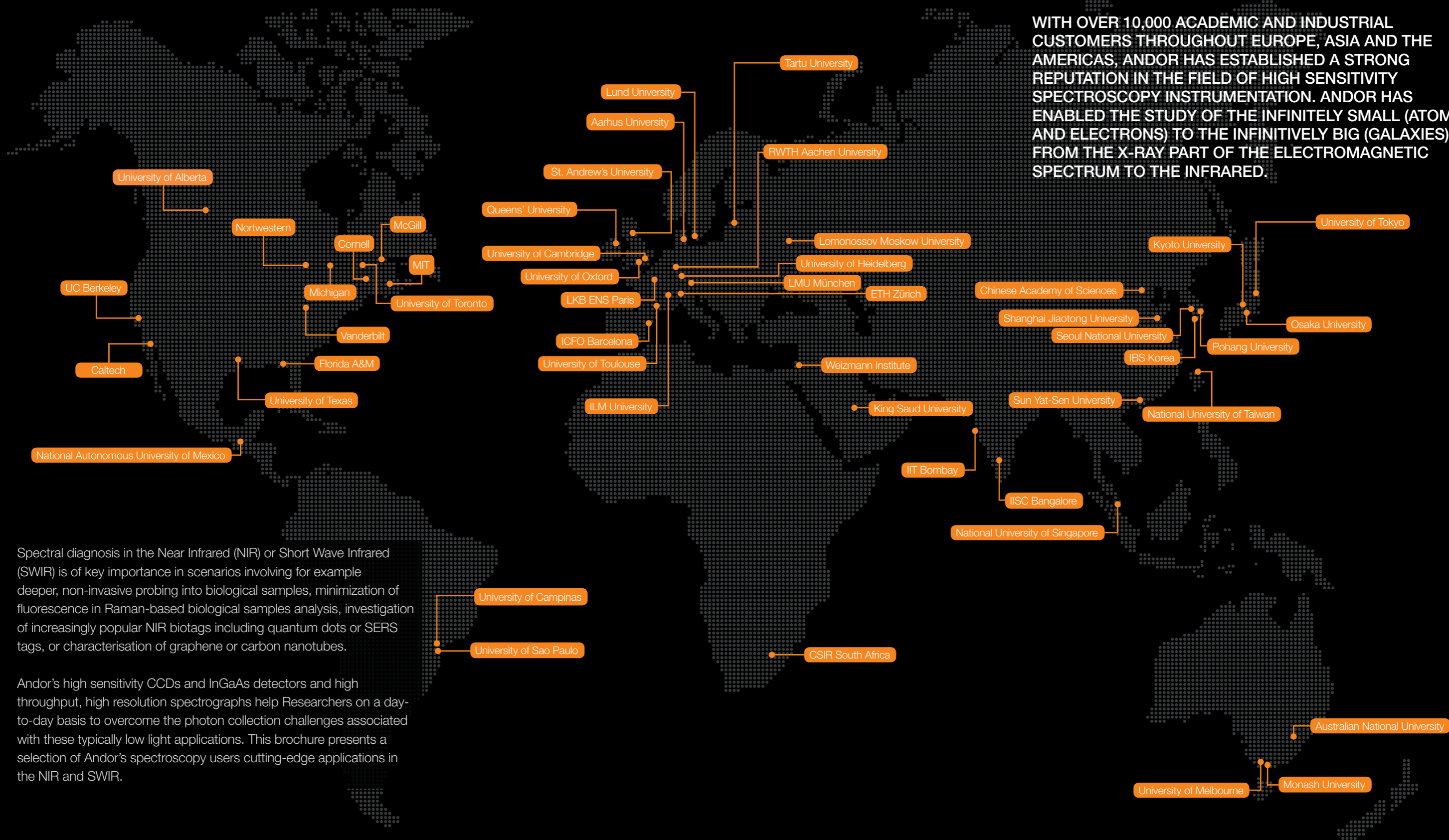
# NIR and SWIR Spectroscopy

## Selected Applications Notes



ANDOR'S HISTORY WITH PHYSICAL SCIENCE - AND IN PARTICULAR OPTICAL SPECTROSCOPY - STARTED IN 1989 AT QUEEN'S UNIVERSITY, BELFAST.

WITH OVER 10,000 ACADEMIC AND INDUSTRIAL CUSTOMERS THROUGHOUT EUROPE, ASIA AND THE AMERICAS, ANDOR HAS ESTABLISHED A STRONG REPUTATION IN THE FIELD OF HIGH SENSITIVITY SPECTROSCOPY INSTRUMENTATION. ANDOR HAS ENABLED THE STUDY OF THE INFINITELY SMALL (ATOMS AND ELECTRONS) TO THE INFINITELY BIG (GALAXIES), FROM THE X-RAY PART OF THE ELECTROMAGNETIC SPECTRUM TO THE INFRARED.



Spectral diagnosis in the Near Infrared (NIR) or Short Wave Infrared (SWIR) is of key importance in scenarios involving for example deeper, non-invasive probing into biological samples, minimization of fluorescence in Raman-based biological samples analysis, investigation of increasingly popular NIR biotags including quantum dots or SERS tags, or characterisation of graphene or carbon nanotubes.

Andor's high sensitivity CCDs and InGaAs detectors and high throughput, high resolution spectrographs help Researchers on a day-to-day basis to overcome the photon collection challenges associated with these typically low light applications. This brochure presents a selection of Andor's spectroscopy users cutting-edge applications in the NIR and SWIR.

# Diagnosis of skin tumors during Mohs micrographic surgery

Dr. Ioan Notingher

School of Physics and Astronomy, The University of Nottingham, UK

Automated imaging and objective diagnosis of excised tissue specimens during cancer surgery is a promising approach for increasing the efficiency of the most advanced surgical procedure. Firstly, this quantitative approach can increase the efficacy of surgery by eliminating the errors related to the subjective inter-observer evaluation of histopathological sections. Secondly, the multimodal spectral histopathology can be applied to tissue sections as well as tissue block, thus eliminating the time-consuming procedures required for preparation of frozen sections required for histopathology.

Basal Cell Carcinoma (BCC) constitutes about 75% of skin cancers with more than 60,000 new patients diagnosed each year in the UK. For aggressive BCCs, Mohs Micrographic Surgery (MMS) is considered the most suitable treatment. Its main disadvantage is the need for frozen section preparation and histopathology examination for all excised tissues, a non-automated, time-consuming technique. These drawbacks lead to an unequal healthcare provision in the UK [1].

To reduce the data acquisition time and make molecular spectroscopy suitable for intra-operative use, a research team at the University of Nottingham has developed novel selective sampling techniques based on multimodal spectral imaging [2]. The team first used tissue auto-fluorescence imaging, which has high sensitivity, high speed and low specificity, to determine the main spatial features of the sample. This information was then used in an automated manner to select and prioritize the sampling points for Raman spectroscopy.

## Experimental Setup

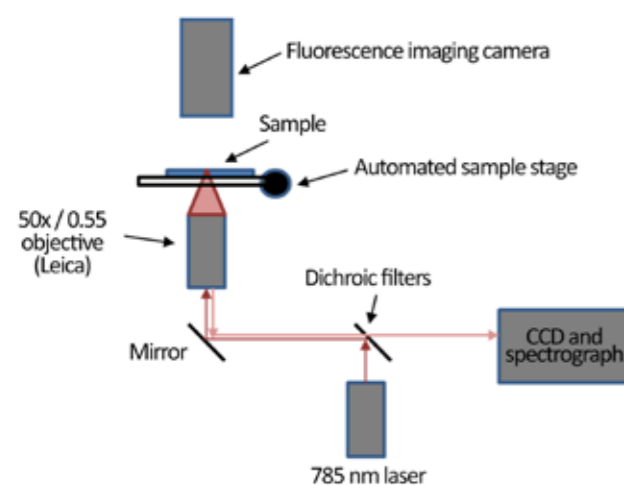


Figure 1: A schematic description of the instrument.

The Raman spectra were recorded using a custom built Raman micro-spectrometer (Figure 1) based on an inverted optical microscope (Eclipse-Ti, Nikon) with a 50x/0.55 objective (Leica), 785 nm wavelength laser (Starbright XM, Torsana), spectrograph (77200, Newport/Oriel), back-illuminated deep-depletion CCD (DU401A-BR-DD, Andor Technology) and automated sample stage (H107 Proscan II, Prior Scientific). The wavelength of the excitation laser was selected to minimize the excitation of tissue auto-fluorescence. The auto-fluorescence images of tissue sections were measured using a wide-field fluorescence imaging system integrated into the Raman microscope; the system consisted of a mercury lamp (Nikon), CCD camera and fluorescence filters for collagen (Semrock, DAPI-5060C-NTE-ZERO) and tryptophan (Semrock FF310-Di01-25x36, FF01-292/ 27-25, FF01-357/ 44-25).

## Results and Discussion

A comparison between multimodal spectral imaging and raster-scanning Raman microscopy is presented in Figure 2. This sampling strategy makes it possible to obtain diagnostic accuracy similar to raster-scanning Raman spectroscopy but with a dramatic decrease in the number of Raman spectra and acquisition time. Accurate diagnosis can be obtained with only 500 - 1,500 Raman spectra for skin samples of 1x1 cm<sup>2</sup> obtained during Mohs surgery, both for tissue sections (Figure 3) and un-sectioned tissue blocks [2].

For the laboratory-based prototype, the acquisition time for the auto-fluorescence images was 4 minutes, integration time for each Raman spectrum was 2 seconds, and the image segmentation processing using a standard PC was 2 minutes. Using these figures, the diagnosis time by MSI can be estimated to 20 - 60 minutes, which even at this early stage is shorter than the frozen section histopathology currently used during MMS (1 - 2 hours).

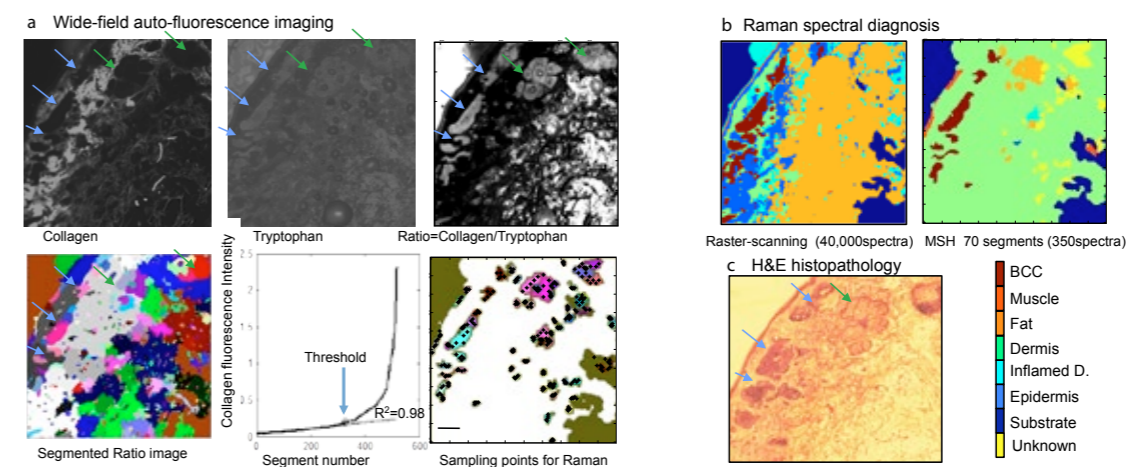


Figure 2: a) The ratio of wide-field auto-fluorescence intensity images corresponding to collagen (exc. 377 nm/em. 447 nm) and tryptophan (exc. 292 nm/em. 357 nm) was analysed by an image segmentation algorithm. The segments eliciting collagen auto-fluorescence intensity above a threshold were classified as dermis and excluded from Raman measurements. For the remaining segments, five sampling points were allocated to each segment based on a space-filling algorithm. b) MSI diagnosis was obtained with only 350 Raman spectra compared to 40,000 for raster scanning. c) H&E histopathology of the adjacent tissue section (tumour indicated by blue arrows) [2].

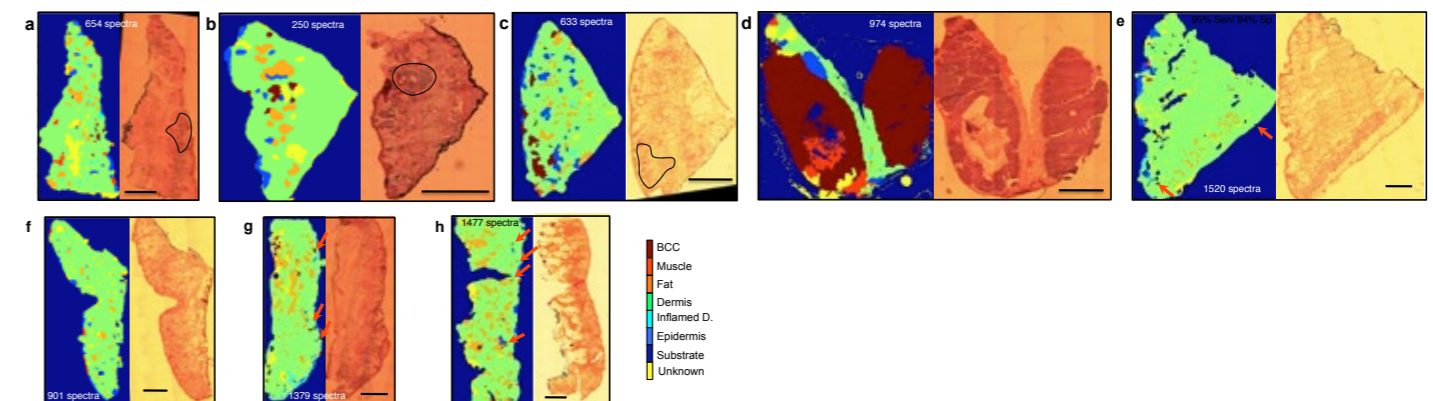


Figure 3: Diagnosis of BCC in tissues removed during Mohs surgery (independent patients): a-e) BCC positive, f-h) BCC-negative. Number of spectra used for the diagnosis is shown for each sample. Scale bar: 2 mm [2].

## Conclusions

These results show the potential of multimodal spectral histopathology for diagnosis of tissues during cancer surgery. This provides a quick and objective way of telling whether the tissue layers removed by the surgeon are clear of tumour or not.

## References

- [1] National Institute for Health and Care Excellence (NICE) 2006, Report on Improving Outcomes for People with Skin Tumours including Melanoma (2006)
- [2] K. Kong, C.J. Rowlands, S. Varma, W. Perkins, I.H. Leach, A.A. Koloydenko, H.C. Williams and I. Notingher, Diagnosis of tumours during tissue conserving surgery with integrated auto- fluorescence and Raman scattering microscopy, PNAS 2013, 110 (38), 15189-15194 (2013)

## Find out more ...



Search for Dr. Notingher's webinar entitled 'Investigating Molecular Properties of Live Cells and Tissues' at [andor.com/learning](http://andor.com/learning)

## Optimizing NIR spectral detection: Back-Illuminated Deep-Depletion iDus and Newton CCD platforms

- ✓ Peak QE up to 95% at 850 nm (BR-DD, LDC-DD)
- ✓ Dual anti-reflection coating option (BEX2-DD) - enhanced broadband detection
- ✓ Thermo-Electric cooling down to -100°C - negligible dark noise
- ✓ Ultravac™ vacuum technology - maintains high quantum efficiency performance year after year
- ✓ Low Dark Current (LDC-DD) option - superior signal to noise ratios in the NIR
- ✓ Fringe-suppression technology - low optical etaloning in the NIR
- ✓ USB connection

# Raman and Photoluminescence measurements on laser lithographically written structures in Si

WITec GmbH, [www.witec.de](http://www.witec.de)

Silicon (Si) plays an important role in semiconductor devices. During manufacturing, the structures in Si are traditionally generated using lithography. Confocal Raman and Photoluminescence (PL) imaging are useful tools for quality assurance to investigate stress and stress-induced artifacts in Si of semiconductor devices. This application note describes the performance of system laser scribing, confocal Raman imaging and confocal PL imaging on a crystalline Si sample with a single microscope system.

Silicon (Si) is the material most widely used for integrated circuits as well as solar cells. Traditionally the structures in these semiconductor devices are produced using lithography. In order to ensure the highest quality, the production steps need to minimize stress and stress-induced artifacts. It has been shown [1,2] that Raman measurements can effectively probe the strain state of crystalline materials and thus provide an effective, non-destructive way of developing the most appropriate production processes. Furthermore stress and crystallinity in Si have a strong effect on the Photoluminescence (PL) signal of the Si [3].

## Results and Discussion

All experiments were performed using an Alpha300 RA Confocal Raman Microscope.

For the lithography experiments the system was equipped with a 532 nm, 15 mW pulsed laser for laser scribing in combination with the DaVinci Lithography package. The lithography process for writing the structure took approximately 2 minutes.

A planar confocal Raman imaging scan in XY direction (50 x 50  $\mu\text{m}^2$ ; 200 x 200 points) was performed on the laser scribed area using an additional 532 nm laser (frequency-doubled Nd:YAG) with 20 mW optical power output. A 100x NA 0.9 objective was used to focus the laser spot to a diameter of 355 nm. The signal was collected with an Andor iDus visible-optimized DV401A-BV with an integration time of 12.2 ms per spectrum.

Following this scan, Figure 1 could be extracted from the integrated intensity of the first order Si band near 520 rel.1/cm. The image shows an increased intensity of the Si signal close to the laser scribed structure as well as a strong decrease exactly along it. The insert shows the color-coded confocal Raman image of the position of the first order Si line (peak shift), highlighting the strained sample areas.

The brighter and darker areas in Figure 1 suggest differences in the height of the sample. In such a case the brighter areas could be lying in an optimal focal plane and the dark areas in planes that are not well in focus. In order to check this, a depth scan in the XZ plane (20 x 5  $\mu\text{m}^2$ ; 200 x 50 points) was performed along the line marked in green in Figure 1. The result can be seen in Figure 2 where the integrated intensity of the first order Si peak is shown. It can be clearly seen that the intensity originates from approximately the same height and that only very little signal is originating from the positions where the laser-scribed structures are located. It can additionally be noted that brighter areas are located right next to the structures. This is in agreement with the results shown in Figure 2.

For confocal PL imaging a specially selected 50x NA 0.8 objective was chosen. This allowed the best throughput for the PL signal in the range of 1000 - 1250 nm for Si while showing minimal chromatic aberration between the excitation wavelength (532 nm) and the PL peak. The detector used in the Short-Wave Infrared region was an Andor iDus InGaAs DU491A-1.7 camera. A confocal PL scan of the laser scribed structures was performed (50 x 50  $\mu\text{m}^2$ , 100 x 100 points, 0.21 s integration time per spectrum). Figure 3a shows the integrated intensity of the Si PL signal and Figure 3b the PL spectrum itself. This spectrum was acquired right in the center of the structure. The second order peak of the excitation wavelength at 1064 nm can also be seen in this spectrum. Since Si is an indirect semiconductor, the PL efficiency is extremely low compared to GaAs material for example. Therefore, only a highly effective detection beam path allows the measurement of the PL signal from a diffraction-limited point with integration times similar to those needed for Raman imaging.

Similar to the confocal Raman image on Figure 1, the intensity of the signal is stronger close to the structures. It has been shown, however, that more elaborate fitting models also allow the extraction of the stress in Si structures from the PL signal [4].

## References

- [1] Gigler A.M., Huber A.J., Bauer M., Ziegler A., Hillenbrand R. and Stark R.W., Nanoscale residual stress-field mapping around nanoindentations in SiC by IR s-SNOM and confocal Raman microscopy. *Optics Express*, 17, 22351-22357 (2009)
- [2] Wermelinger T., Borgia C., Solenthaler C. and Spolenak R., 3-D Raman spectroscopy measurements of the symmetry of residual stress fields in plastically deformed sapphire crystals. *Acta Materialia*, 55, p4657-4665 (2007)
- [3] Gundel P., Schubert M.C. and Warta W., Simultaneous stress and defect luminescence study on silicon. *Phys. Status Solidi A*, 207, 436-441 (2009)
- [4] Dieing T. and Holtricher O., High-resolution, high-speed confocal Raman imaging, *Vibrational Spectroscopy* 48; p22-27 (2008)

## Figures and Figure Captions

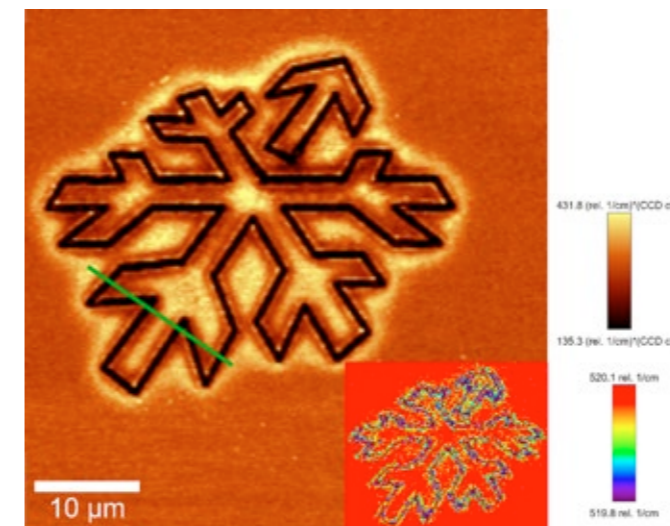


Figure 1: Confocal Raman image of the intensity of the first order Si line. The green line indicates where the depth scan was performed. The insert shows the confocal Raman image of the position of the first order Si line in the planar scan (peak shift).

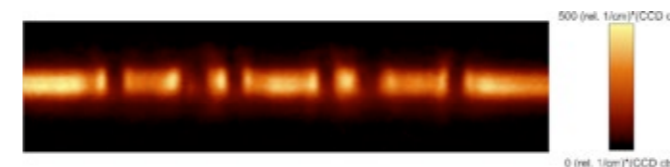


Figure 2: Confocal Raman Image of the intensity of the first order Si line along a depth scan.

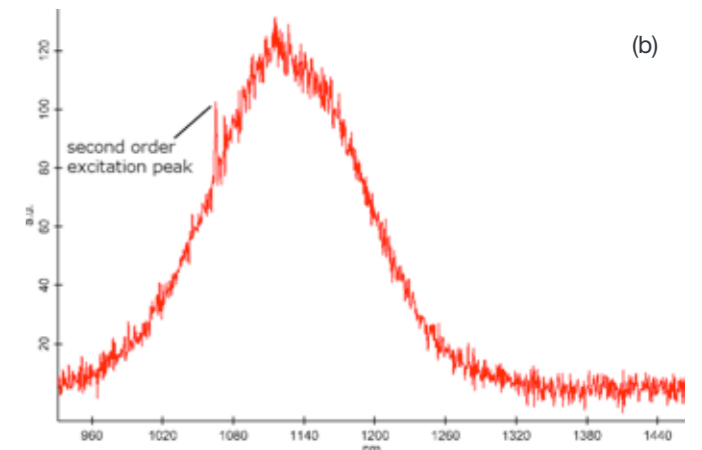
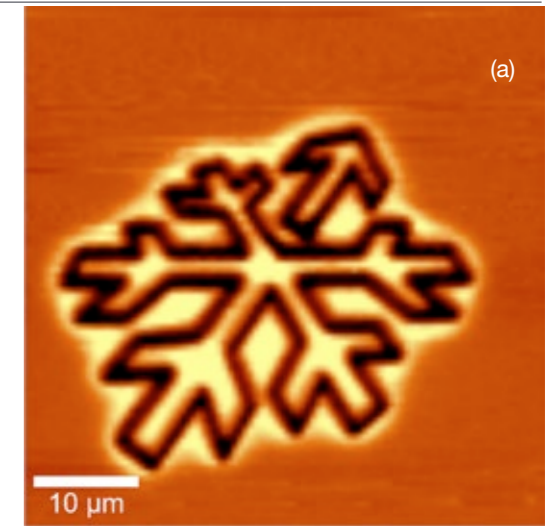


Figure 3: Confocal PL image of the intensity of a PL signal in a planar scan (a) and a representative PL spectrum which originates from the center of the structure (b).

## Learn more about InGaAs detectors - is cooler really better?

Andor iDus InGaAs series can be Thermo-Electrically (TE) cooled down to -90°C, allowing access to the best signal-to-noise (SNR) performance without the inconvenient use of LN<sub>2</sub>.



Beyond this cooling point, blackbody radiation from any elements facing the sensor will dominate the 'dark signal', and Quantum Efficiency will be impacted with decreasing cooling temperature, which may result in lower SNR performance.



Search for the webinar entitled 'A TE Cooling Approach to SWIR' at [andor.com/learning](http://andor.com/learning)

# Measurement of OH airglow temperatures in the mesopause region

C. Schmidt, M. Bittner  
German Aerospace Center, Oberpfaffenhofen, Germany

The German Remote Sensing Data Center (DFD) of the German Aerospace Center (DLR) operates ten Infrared-Spectrometers GRIPS (ground-based infrared p-branch spectrometers) for routine observations of the so-called airglow originating from the upper mesosphere / lower thermosphere region. In this region atomic hydrogen reacts with ozone to form molecular oxygen and hydroxyl molecules.

## Introduction

The excess energy of the exothermic reaction  $O_3 + H \rightarrow O_2 + OH^*$  (+ 3.32 eV) is mainly transferred into rotational and vibrational excitations of the OH-molecules (denoted by \*). These OH\*-molecules form a layer of about 8 km thickness at a peak altitude of about 87 km. Returning to their ground state, the OH\*-molecules emit infrared radiation in the spectral region between ca. 710 nm and 2500 nm. The brightness of this OH\*-airglow varies between  $10^{-6}$  to  $10^{-4}$  Wm<sup>-2</sup>sr<sup>-1</sup>, making it the brightest phenomenon at the night sky (Leinert *et al.*, 1998).

Since the deactivation of the OH\* takes place by a large number of successive rotational-vibrational transitions, the low energy transitions are supposed to be in local thermodynamic equilibrium with the surrounding atmosphere. It is therefore possible to derive the rotational temperature as an estimator of the kinetic temperature at this height by measuring the intensities of several rotational lines within the same vibrational branch. The measurements performed by the German Remote Sensing Data Center are a contribution to the global Network for the Detection of Mesopause Change (NDMC, <http://wdc.dlr.de/ndmc>). The mission of this program is to promote international cooperation among research groups investigating the mesopause region (80-100 km), with the main goal of early identification of changing climate signals.

One of the major topics of scientific interest in middle atmosphere research is the investigation of atmospheric dynamics on all time scales. This includes the study of climate trends over several decades as well as the characterization of different atmospheric waves. Depending on their nature these waves are categorized as planetary, gravity and infrasonic waves. Their corresponding typical periods range from days to weeks for planetary waves, several minutes to many hours for atmospheric gravity waves and less than 5 minutes in case of infrasonic waves (e.g. Pilger and Bittner, 2009).

## Setup

While Meinel (1950) relied on exposure times of more than 40 hours for his discovery of the airglow phenomenon in the late 1940s, the application of an InGaAs-array detector (Andor iDus DU490A-1.7) in combination with a high aperture spectrograph (Andor Shamrock 163) now allows exposure times as low as 10 to 15 seconds. This temporal resolution is considerably higher than what was previously achieved with scanning spectrometers equipped with liquid nitrogen cooled low noise Germanium photodiodes.

The thermoelectric cooling system of the iDus DU490A-1.7 constitutes an important advantage over liquid nitrogen cooled systems in terms of robustness and maintenance requirements. Therefore eight out of ten spectrometers currently operated by the German Remote Sensing Data Center are equipped with the iDus DU490A-1.7.



Figure 1: Setup of the GRIPS 6 instrument at the German Remote Sensing Data Center in Oberpfaffenhofen (48.09°N / 11.28°E). The instrument is composed of an Andor Shamrock 163 spectrograph, an Andor iDus DU490A-1.7 photodiode array, powered by a PS-25 power supply for deep cooling temperatures in combination with an Exos-2 water recirculator. The laptop shows a 15 s exposure of the OH nightglow between 1500 to 1600 nm obtained with the Andor Solis software.

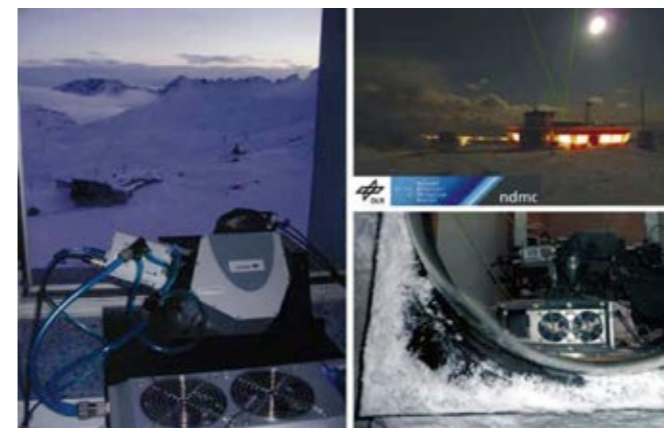


Figure 2: The left panel shows the GRIPS 5 instrument deployed at the Environmental Research Station "Schneefernerhaus" (47.42°N / 10.98°E), located 2650 m above sea level on Germany's highest mountain Zugspitze. The right panels show the setup of the GRIPS 9 instrument under a dome on top of the roof of the Arctic Lidar Observatory for Middle Atmosphere Research (ALOMAR, 69.28°N / 16.01°E) in Norway during winter 2010/2011.

The Exos-2 water recirculator efficiently helps stabilize the temperature of the detector, even in rather warm environments of +30 °C or more. During routine observations the grating is placed at a fixed angle and the spectral region between 1500 and 1600 nm is dispersed across the 512 pixel InGaAs-array. While some of the GRIPS instruments are equipped with special entrance optics, others are simply mounted in an upward direction to observe the night sky (see Figure 1). Their field of view is thereby determined by the F-number of the Shamrock 163 (F/# = 3.6). The most important feature of the iDus DU490A-1.7 in its application to airglow observation is the fact that the detectors dark current, which are an order of magnitude lower than the recorded airglow signal, are very stable throughout the night, allowing accurate measurements of the emission lines' intensities.

## Results and Discussion

The GRIPS 5 and GRIPS 6 instruments were the first to be equipped with the iDus DU490A-1.7 in October 2008 and January 2009 respectively. Since then they have been performing routine measurements almost every night. Until April 2011 the GRIPS 6 had been operated during more than 750 nights, with the camera taking data between 7 hours (summer) and 15 hours (winter) each night. No significant change in responsivity of the system was observed within these two years.

The low maintenance requirements of the systems also facilitate the remote operation of spectrometers placed at distant sites, such as the Environmental Research Station "Schneefernerhaus" (47.42°N/10.98°E), located on Germany's highest mountain Zugspitze and the Arctic Lidar Observatory for Middle Atmosphere Research (ALOMAR, 69.28°N/16.01°E) in Norway (Figure 2). New observation sites throughout Europe and beyond are currently in preparation. Data obtained with these instruments can be accessed in near real time via the World Data Center for Remote Sensing of the

Atmosphere (WDC-RSAT, <http://www.wdc.dlr.de/ndmc>).

Figure 3 shows a typical spectrum obtained with the GRIPS 8 at an exposure time of 15 seconds during the night from February 5<sup>th</sup> to 6<sup>th</sup>, 2011 at the Environmental Research Station "Schneefernerhaus". During routine observations one spectrum is obtained every 15 seconds. Thus, the amount of spectra obtained each night ranges between 1800 (summer) and 3600 (winter) for the observation sites in Germany and up to 5000 spectra during winter conditions at ALOMAR (69.28°N/16.01°E) in Norway.

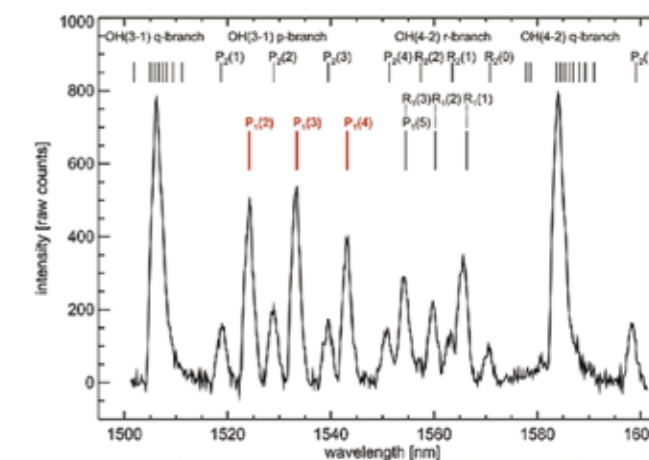


Figure 3: Medium resolution OH\*-airglow spectrum between 1500 and 1600 nm; the original OH-linewidth is less than 0.01 nm. The spectrum was obtained with the iDus DU490A-1.7 detector mounted on the Shamrock 163 with the slit width set to 250 μm. The detector was operated in high sensitivity mode, at a cooling temperature of -60°C and an exposure time of 15 seconds. The dark current of approximately 5000 counts per pixel was background subtracted. The three P1-lines of the OH<sub>v=3-1</sub> branch are used for the calculation of rotational temperatures. This particular spectrum yields a temperature of 213.6 K ± 3.5 K. The uncertainty is estimated from the signal-to-noise ratio, which is rather high for this kind of measurement. For comparison, the photon flux is of the order of approximately 5000 photons s<sup>-1</sup>arcsec<sup>-2</sup>μm<sup>-1</sup> at the maxima of the two Q-branches (Leinert *et al.*, 1998); the field of view of the instrument is approximately 15° full angle.

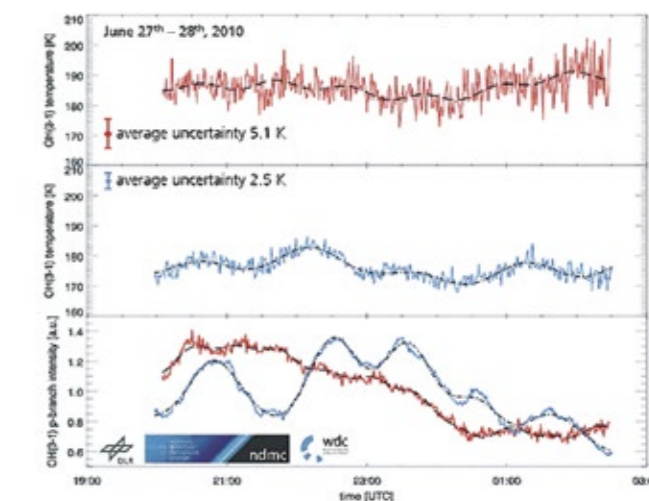


Figure 4: Simultaneous measurements performed with the GRIPS 6 instrument at Oberpfaffenhofen (red) and with the GRIPS 7 at the Schneefernerhaus (blue), both in Southern Germany. The field of views in the mesopause region are approximately 200 km apart.

Figure 4 shows the nocturnal evolution of OH\* rotational temperatures and intensities for the night from June 27<sup>th</sup> to 28<sup>th</sup>, 2010, recorded simultaneously at two sites in Southern Germany. Both instruments captured rather strong oscillations in both airglow intensity and rotational temperature. It is important to note, that intensities and temperatures constitute independent parameters in airglow observations (temperatures depend on relative line intensities, not on absolute intensities). Therefore, oscillations in temperature and intensities are usually not in phase.

The upper panels show the evolution of one minute mean values of rotational temperatures, the lower panel shows the respective airglow intensity variation at both sites. The black curves denote the dominant oscillations, which are retrieved applying a spectral analysis (harmonic analysis) to the data. During that night the wave activity differed significantly at both stations. A 2.2 hour (gravity) wave, which is clearly seen in the intensity variations at the Schneefernerhaus (lower panel, blue), can also be found in the data from Oberpfaffenhofen (lower, panel red), but its amplitudes are decreased by more than 60%.

Finally, Figure 5 shows the evolution of nocturnal mean values since the start of observations in Oberpfaffenhofen on January 29<sup>th</sup>, 2009 to April 4<sup>th</sup>, 2011. The outstanding performance of the instrument resulted in the successful retrieval of nocturnal mean temperatures for 80% of all nights – a unique value for a mid latitude observation site. This excellent coverage is owed to the fact that the initial high temporal resolution allows researchers to take advantage of small gaps in cloud coverage in order to collect enough data, at least two hours, for a representative nightly mean, even during nights with rather poor viewing conditions.

## References

[1] Bittner, M., K. Höppner, C. Pilger and C. Schmidt, Mesopause temperature perturbations caused by infrasonic waves as an early indicator for the detection of tsunamis and other geo-hazards. *Natural Hazards and Earth System Sciences* 10, p1431-1442 (2010)

[2] Leinert, Ch., Bowyer, S., Haikala, L.K., Hanner, M.S., Hauser, M.G., Levasseur-Regourd, A.-Ch., Mann, I., Mattila, K., Reach, W.T., Schlosser, Staude, H.J., Toiler, G.N., Weiland, J.L., Weinberg, J.L. and Witt, A.N.: The 1997 reference of diffuse night sky brightness. *Astronomy and Astrophysics Supplement Series* p127, 1-99 (1998)

[3] Meinel, A.B., OH Emission Bands in the Spectrum of the Night Sky. *Astrophysical Journal* 111, p555-564 (1950)

[4] Pilger, C. and M. Bittner, Infrasound from tropospheric sources: Impact on mesopause temperature? *Journal of Atmospheric and Solar-Terrestrial Physics* 71, p816-822 (2009)  
NDMC: <http://wdc.dlr.de/ndmc>

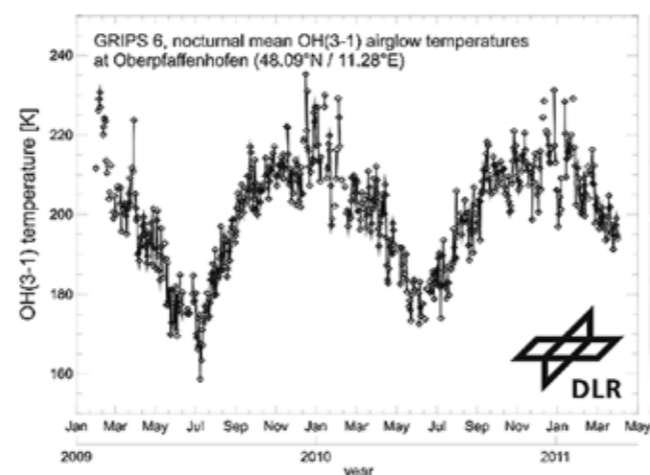


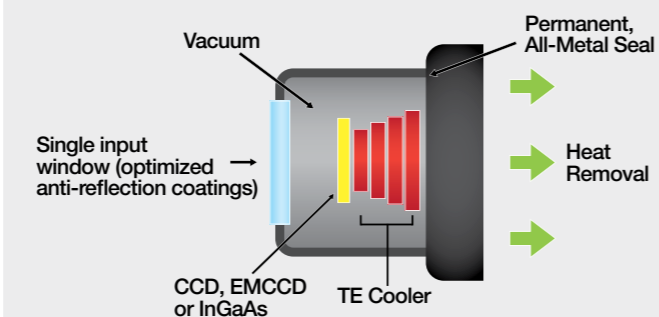
Figure 5: Course of nocturnal mean OH\* -airglow temperatures since the beginning of measurements at Oberpfaffenhofen on January 29<sup>th</sup>, 2009. For 629 nights (80% of the complete observation time) a nocturnal mean value was successfully retrieved, only a minor fraction was lost due to bad weather. As a consequence of the high temporal resolution, a large number of spectra contribute to the nocturnal means resulting in a statistical uncertainty, which is less than 1 K for every value shown here. The upper atmospheric residual circulation causes low temperatures during summer and high temperatures during winter. The strong day to day variation is mainly caused by so-called planetary waves.

Schneefernerhaus: <http://www.schneefernerhaus.de/en/>  
ALOMAR: [http://www.rocketrange.no/?page\\_id=19](http://www.rocketrange.no/?page_id=19)

## Benefits of Ultravac™ technology for research-grade cooled detectors

Unless protected, cooled CCD, EMCCDs or InGaAs sensors will condense moisture, hydrocarbons and other gas contaminants. Exposed to such outgassed contaminants when cooled, the Quantum Efficiency of sensors will decline proportionally. Andor's Ultravac™ offers the following benefits:

- ☑ Maintenance-free operation in-laboratory or in-field over extended periods of time, unlike liquid nitrogen (LN<sub>2</sub>) cooled platforms that require hazardous and regular manual Dewar refills.
- ☑ Operating temperature of the chip can be reduced significantly. Better cooling with an enhanced thermoelectric (TE) Peltier design translates into substantially lower darkcurrent and fewer "hot" blemishes.
- ☑ No peak QE and sensor cooling performance degradation over many years operation. Andor Ultravac™ technology offers an MTBF (mean time between failure) of more than 100 years.



# Spectral Flow Cytometry expanded to Visible and Near Infrared Fluorescence Spectroscopy

John P. Nolan  
La Jolla Bioengineering Institute, San Diego, California, USA

The inherent design of a flow cytometer gives a unique advantage in multiparameter measurements on single particles, where each fluorophore is matched to a unique detector. However, the long standing goal of collecting complete emission spectra of spectrally labeled particles has remained elusive. In recent years Professor John Nolan and his group at the La Jolla Bioengineering Institute in San Diego have made significant strides toward this goal by coupling high-throughput dispersive spectrometers to standard design flow cytometers.

## Introduction

The Nolan group has developed a Spectral Flow Cytometer (SFC) capable of acquiring complete emission spectra of single particles by substituting a dispersive optic spectrometer in place of the traditional mirrors, filters and photomultipliers (PMTs) on a conventional flow cytometer. A key component of the SFC is a high speed, multi-element CCD detector, which enables the collection of a complete high resolution spectrum during the short transit time of an individual cell through the instrument probe volume. The measurement is enhanced over traditional flow cytometers by the high sensitivity of these detectors, especially in the near infrared (NIR) spectral region, and by the on-chip binning capability which allow for signal enhancement, while minimizing noise. The coupling of the highly sensitive detector with a high throughput imaging spectrograph allows for a measurement time approaching 200 events per second.

## Setup

The Nolan group's first generation SFC featured a collection and detection system capable of distinguishing particles using Surface Enhanced Raman Spectroscopy (SERS) [1]. Raman spectroscopy is well suited to multi-parameter measurements due to the availability of narrow spectral features in a relatively small spectral window. The Raman flow cytometry instrument has been shown capable of characterizing the Raman active population of bulk nanoparticle preparations at a single nanoparticle level [2]. This allowed for the optimization of the SERS tagged nanoparticle synthesis to produce bulk preparations with a large percentage of nanoparticles featuring high Raman activity. More recently, the system has been used to distinguish populations of cells labeled with two different SERS tagged antibodies [3]. The Raman spectral flow cytometer is well suited to address many of the common applications in flow cytometry, however fluorescent tags are most often used as a labeling

agent. Therefore a system capable of distinguishing the relatively broad emission of visible and near-infrared emission probes was necessary.

To this end, the Nolan group has developed two second generation SFCs (Figure 1) [4]. The first is configured for visible fluorescence detection and is based on an optical bench from a commercially available flow cytometer (FACSCanto, BD Biosciences). Excitation by either a 488 nm or 405 nm laser is directed to the flow cell by the flow cytometer beam steering and shaping optics. The spectral detection system consists of a fiber-coupled HoloSpec imaging spectrograph with either 457 nm edge filter or a 488 nm notch filter and a broadband volume phase holographic grating coupled to a Newton DU970-UVB EMCCD detector. The second system is similar to the Raman flow cytometer previously described [1] but is configured for NIR fluorescence and uses a 785 nm diode laser for excitation. The emitted light is fiber coupled to a HoloSpec imaging spectrograph with a 785 nm edge filter, a narrow band volume phase holographic grating and a Newton DU920N-BRDD for the detection. On both systems spectral detection was triggered using the forward angle light scattering (FALS) detection system of the respective optical bench.

The use of a dispersive optic based, high throughput spectrograph with a highly sensitive CCD detector offers increased multiplexing capability over conventional flow cytometers. But, in order to realize the benefit of the increased data into multi-parameter cell and particle based applications, spectral unmixing data analysis routines are required. The Nolan group applied two spectral unmixing approaches to the fluorescence spectral flow cytometry data. The first replicates a traditional flow cytometer with optical filters for spectral separation. Digital filters are applied in post-acquisition analysis in order to separate the different spectral components of the total signal. This offers a huge advantage over the traditional method since the number of filters is limited only by the number of spectral data

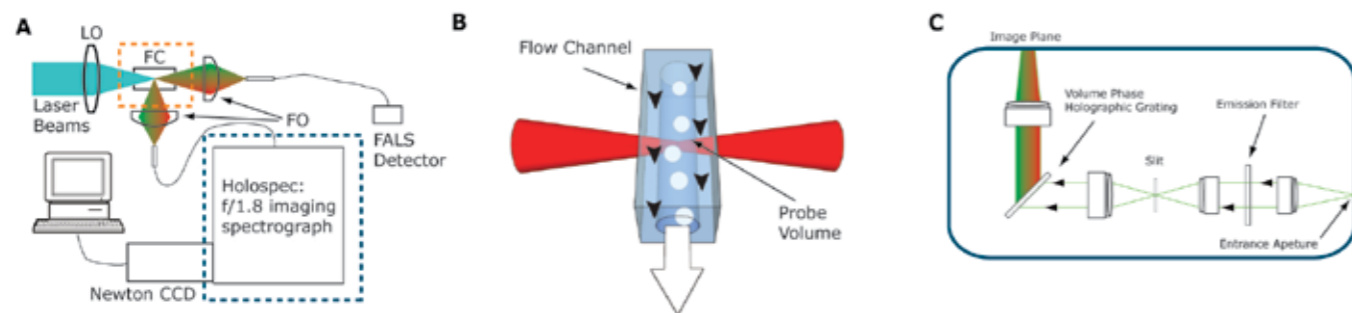


Figure 1: The Spectral Flow Cytometer. A) Schematic of the SFC: 405, 488, or 785 nm laser emission is directed at the flow chamber (FC) by laser focusing and shaping optics (LO). Fluorescence is collected by fiber coupling optics (FO) and directed at either the FALS detector, a traditional PMT based detector (not shown) or a dispersive imaging spectrograph. The dispersed spectrum is detected by either a Newton EMCCD or a Newton BRDD CCD camera. B) Sample is hydrodynamically focused to flow as a straight line through the focus laser excitation beam. C) Schematic of the HoloSpec spectrograph: fiber coupled light is collimated by a lens before being passed through a notch or edge filter, the filtered light is focused through a slit and recollimated before being directed on to a volume phase holographic grating. The spectrally dispersed light is then focused onto the camera.

points and each filter can be tuned to exactly match the emission spectra of the fluorescence dyes. Even so, the power of this spectral filter analysis is limited, since the broad spectral features typical of fluorescent dyes ensure a significant amount of cross talk between adjacent filters for dyes with similar emission spectra. The second approach uses a custom nonnegative classical least squares (CLS) routine. This approach assumes that the detected signal from a mixture of fluorescent dyes is a linear combination of the individual spectra of the components. Using this approach, spectral unmixing can clearly identify fluorescent tags even when a high degree of spectral overlap is present.

## Results and Discussion

In order to characterize the ability of the SFC to distinguish particles with fluorescent labels, the Nolan team measured microspheres labeled with one of six different quantum dots using the instrument optimized for visible detection, (Figure 2). Using the custom CLS routines, the spectral flow cytometer could not only uniquely identify the label on each microsphere but could determine the amount of each

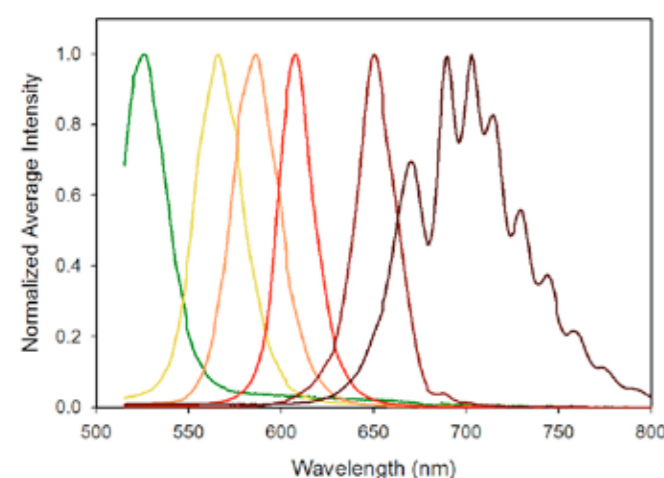


Figure 2: Average spectra of single beads stained with following Qdots: QD525, QD565, QD585, QD605, QD655, and QD705. The average fluorescence intensity has been normalized to average peak intensity of each individual Qdot.

component present. Additionally the spectral mixing routine can account for differences in the absolute brightness of the six different tags, thereby providing the basis for quantitative fluorescently labeled antibody measurements. Next, the team measured mixtures of two, three, four, five and all six of the quantum dot labeled microspheres and successfully identified each component and the relative abundance of all 5 mixtures. Finally, the technique was applied to a common flow cytometry application, the analysis of PBMCs stained with canonical surface markers used in lymphocyte subsetting. The spectral flow cytometer with CLS unmixing was able to distinguish CD14+ monocytes and CD3+ T cells as well as the CD4 and CD8 positive subsets demonstrating the instruments capability in “real-world” applications.

Traditional flow cytometers struggle with spectral detection in the red and near-infrared spectral regions primarily due to the rather poor performance of PMT’s (Quantum Efficiency = 2-8%) in this region. The use of a back-illuminated deep depletion (BRDD) detector on a dispersive spectrometer will allow the SFC to take advantage of the increasing availability of fluorescent dyes with emission in this spectral window. In order to probe the possibilities of near-infrared fluorescence applications in spectral flow cytometry, the Nolan group characterized seven different fluorescently labeled microspheres with emission in the NIR. Of the seven dyes tested, three (Alexa 750, Cy7.5, and DyLight 830) gave spectra with enough distinction to allow for unique determination with CLS unmixing, (Figure 3). The results are indicative of a promising future for spectral flow cytometry in near infrared spectral region, with dyes already available commercially. The increase in development of bright dyes with far-red to near-infrared emission should ease the use of this spectral region in flow cytometry applications in the near future.

## References

[1] Watson, D.A., Brown, L.O., Gaskill, D.F., Naivar, M., Graves, S.W., Doorn, S.K., and Nolan, J.P., ‘A Flow Cytometer for the Measurement of Raman Spectra,’

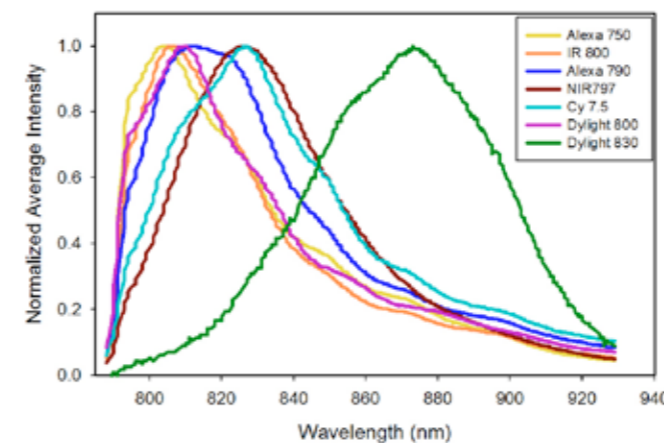


Figure 3: Average spectra of single beads stained with the following near infrared fluorophores: Alexa 750, IRDye800, DyLight 800, Cy7.5. The average fluorescence intensity has been normalized to the average peak intensity of each individual QDot.

Cytometry Part A, Vol 73A, p119-128 (2008)

[2] Sebba, D.S., Watson, D.A., Nolan, J.P., High Throughput Single Nanoparticle Spectroscopy, ACS Nano, Vol. 3 No. 6, p1477-1484 (2009)

[3] Nolan, J.P., Duggan, E., Liu, E., Condello, D., Dave, I., Stoner, S.A., Single Cell Analysis Using Surface Enhanced Raman Scattering (SERS) Tags, Methods Vol 57, p272-279 (2012)

[4] Nolan, J.P., Condello, D., Duggan, E., Naivar, M., Novo, D., Visible and Near Infrared Fluorescence Spectral Flow Cytometry. Cytometry Part A. Vol. 83, No. 3, p253-264 (2013)

## Learn more about the ultrafast Newton back-illuminated deep-depletion CCD platform



- Peak QE up to 95% at 850 nm
- Dual anti-reflection coating option (BEX2-DD) - enhanced broadband detection
- Thermo-Electric cooling down to -100°C - negligible dark noise
- Ultravac™ vacuum technology - maintains quantum efficiency performance year after year
- Fringe-suppression technology - low optical etaloning in the NIR
- Acquisition speed over 1,600 spectra per second in Crop Mode
- USB connection

## Learn more about the ultrafast Newton back-illuminated Electron Multiplying (EM) CCD platform for ultra low-light, ultrafast Spectroscopy in the Visible

- < 1 e- readout noise and peak QE up to 95% at 550 nm - single photon sensitivity
- Thermo-Electric cooling down to -100°C - negligible dark noise
- Acquisition speed over 1,500 spectra per second in Crop Mode
- USB connection

## For more information ...



Search for ‘EMCCD for Spectroscopy’ at [andor.com/learning](http://andor.com/learning) or visit [andor.com/newton](http://andor.com/newton)

# NIR micro-photoluminescence characterization of Single semiconductor Quantum Wires

Benito Alén, Juan Martínez Pastor  
Instituto de Microelectrónica de Madrid (CNM, CSIC), Spain

Nanoscale structures (quantum dots and quantum wires) are being studied extensively with a view to building ever more exotic devices, such as more efficient lasers and LEDs, or quantum information processing components. One type of material under investigation consists of semiconductor quantum wires based on InAs.

## Introduction

These are being explored because of their near-infrared optical properties. Work reported by Dr Benito Alén and co-workers [3] on fundamental studies of isolated InAs nanowires (QWRs) identifies novel behavior based around the metal-insulator transition in correlated electron systems. They made use of NIR photoluminescence (NIR-PL) to explore the transition dependencies on both excitation power and temperature.

The analysis of the photoluminescence of individual semiconductor quantum wires is an invaluable tool to investigate the role played by attractive and repulsive Coulomb interactions among electrons and holes confined to one dimension. In these systems, the electronic and optical properties change dramatically depending on the number of trapped carriers, but the effect on the emission spectrum can be obscured if many QWRs with different sizes contribute to the emitted light. To ascertain the physics behind and confront the experimental data against existing theories, the photons emitted from just one QWR must be examined using high spatial resolution techniques and high sensitivity light detectors. This approach has been demonstrated for InAs/InP QWRs emitting at 1.5  $\mu\text{m}$ , by researchers in Spain at the Consejo Superior de Investigaciones Científicas (CSIC) and the Universidad de Valencia.

The prediction of low threshold for laser emission, reduced temperature sensitivity, and slow surface recombination velocity has largely motivated the research on III-V semiconductor QWRs for optoelectronic applications in recent years. Among them, self assembled InAs/InP QWRs can get their spontaneous emission tuned beyond 1.6  $\mu\text{m}$  and their areal density reduced down to a few QWRs per square micron [1]. They are therefore ideal candidates for the fabrication of advanced light sources in the telecom spectral region [2], and for the study of novel semiconductor physics. For the latter, collective phenomena of one-dimensional excitons have been

directly investigated in these nanostructures using NIR microphotoluminescence ( $\mu\text{-PL}$ ) techniques at low temperatures, at the Universidad de Valencia and published by B. Alén *et al.* in Physical Review Letters [3].

## Setup

The system consisted of a fibre-based confocal microscope arrangement inserted in the exchange gas chamber of an immersion liquid He cryostat. Excitation light from a 950 nm diode laser was brought into the microscope through a single mode optical fibre whose core acted as the excitation pinhole. The laser light was focused onto the sample through an objective lens (NA=0.55) producing a diffraction limited spot at the excitation wavelength. Light emitted NIR micro-photoluminescence characterisation of Single semiconductor Quantum Wires Nanoscale structures (quantum dots and quantum wires) are being studied extensively with a view to building ever more exotic devices, such as more efficient lasers and LEDs, or quantum information processing components. One type of material under investigation consists of semiconductor quantum wires based on InAs. The few QWRs present in the excitation spot (see AFM image in Figure 1) were collected by the same objective and

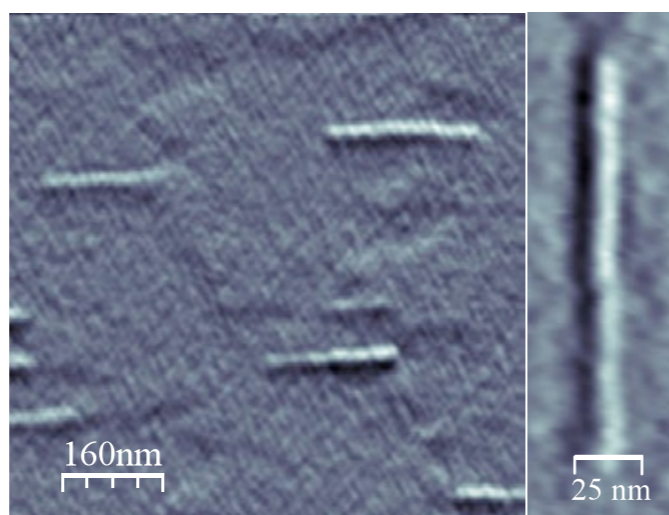


Figure 1: AFM image of the investigated QWRs (Courtesy Dr B Alén, CSIC, Madrid)

focused onto a different optical fibre, which in turn was connected at its opposite end to a spectrometer equipped with a TE cooled Andor iDus InGaAs (DU490A-1.7) camera. The faint light emitted from the individual QWRs could be detected using exposure times of 10 to 100 seconds thanks to the multichannel detection capabilities of the iDus InGaAs array and low dark current of the cooled array. The samples were made using self-assembly methods of epitaxially growing InAs structures on InP (001) substrates under conditions which preferentially led to the formation of QWRs rather than quantum dots (QDs). Reflection highenergy electron diffraction (RHEED) and Atomic Force Microscopy (AFM) analyses were used to characterize the morphology and aspect ratio of the individual QWRs. These structures were typically 20 nm wide and 200 nm long, corresponding to aspect ratios of  $\sim 1:10$ .

## Results and Discussion

Experiments were carried out to investigate how the samples behaved with variation in the excitation power, with powers as low as 8 mW up to 260 mW. They also investigated the temperature dependence.

Typical examples of  $\mu\text{-PL}$  spectra collected on a single QWR as a function of excitation power density are depicted in Figure 2. Due to the quantum confinement size effect, the different sized QWRs can emit at different energies, but they show a similar trend with the increasing photo-generated carrier density. The analysis of the line shape of several spectral features observed at low and high excitation allowed a detailed study of the metal-insulator transition governed by enhanced Coulomb correlations in these systems. At low powers

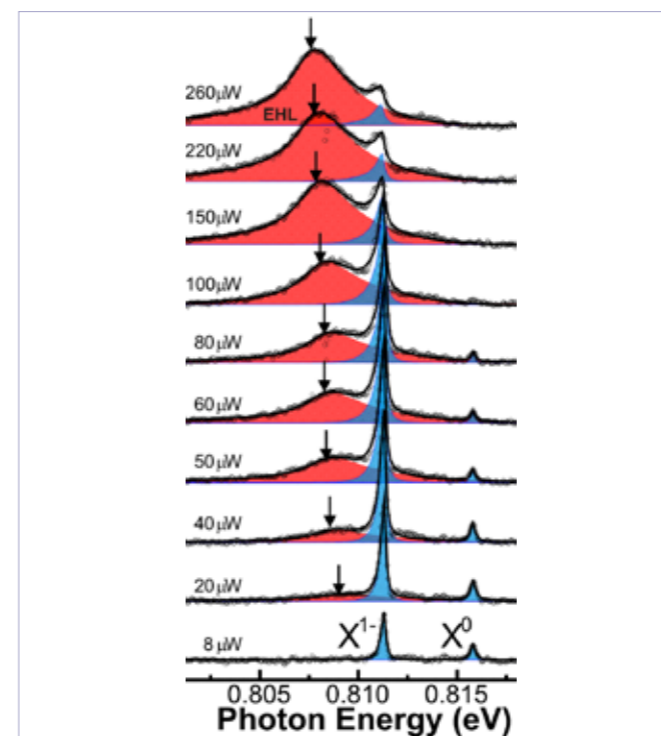


Figure 2: Typical single QWR emission spectra measured at 5 K with increasing excitation power. (Courtesy Dr B Alén, CSIC, Madrid)

the sharp spectral feature at  $\sim 0.812$  eV ( $\sim 1528$  nm) dominated whilst at high powers the broad spectral feature centred at  $\sim 0.807$  eV ( $\sim 1538$  nm) dominated. This change in PL emission, induced by changes in carrier density, was indicative of the metal-insulator transition.

The spectra show that the insulating excitonic gas (associated with high energy peaks – blue) condenses into a metallic-like electron-hole liquid phase (associated with the low energy band - red), with an increase in carrier density.

Novel behavior on the metal-insulator transition within a correlated electron system, as realized in single InAs/InP QWRs emitting in the NIR, was clearly demonstrated by Alén and co-workers. They developed techniques based on  $\mu\text{-PL}$ , which allowed exploration of the carrier interactions and its dependence on photo-excitation powers and temperature. These fundamental studies will underpin future developments of ever more exotic devices such as high efficiency micro-/nano-lasers and LEDs.

## References

- [1] D. Fuster, B. Alén, L. González, Y. González and J. Martínez-Pastor, Initial stages of self-assembled InAs/InP(0 0 1) quantum wire formation. Journal of Crystal Growth 301, 705 (2007)
- [2] L. J. Martínez, B. Alén, I. Prieto, D. Fuster, L. González, Y. González, M. L. Dotor, and P. A. Postigo, Room temperature continuous wave operation in a photonic cristal microcavity laser with a single layer of InAs/InP self-assembled quantum wires. Optics Express 17, 14993 (2009)
- [3] B. Alén, D. Fuster, G. Muñoz-Matutano, J. Martínez-Pastor, Y. González, J. Canet-Ferrer and L. González, Exciton Gas Compression and Metallic Condensation in a Single Semiconductor Quantum Wire. Phys. Rev. Lett. 101, 067405 (2008)

## The Andor InGaAs Series

- ☑ 1.7  $\mu\text{m}$  and 2.2  $\mu\text{m}$  cutoff options - peak QE > 80% and 70% respectively
- ☑ Thermoelectric cooling down to  $-90^\circ\text{C}$  and Ultravac™ vacuum technology - maintenance-free operation, QE performance guaranteed year after year
- ☑ Minimum exposure time of 1.4  $\mu\text{s}$  - increased fast transient phenomena sampling
- ☑ 12.5 and 25.6 mm wide arrays option
- ☑ USB 2.0 plug and play connectivity





# Non-invasive Quality Control of Cryopreserved Samples

Heiko Zimmermann

Biophysics and Cryotechnology Department, Saarland University, Germany

Since the dawn of modern medicine, human biological material has been collected for a variety of purposes. Should the material be collected for diagnostic purposes, it is often possible to be satisfied with a relatively short shelf-life. However, many unique samples are collected and stored for later use and we have witnessed rapid growth in the demand for biobanking in reproductive and regenerative medicine, tissue engineering, stem-cell and cell biology, and pharmaceutical research. In almost all cases, blood and plasma being the most common exceptions, biological integrity throughout the long-term storage is ensured by cryopreservation at temperatures below  $-137^{\circ}\text{C}$ .

## Introduction

These samples may be unique and virtually irreplaceable, but many of these specimens have been lost, and continue to be lost, through thermal damage. Any testing for physiological and genetic soundness before their use is likely to render them unfit for subsequent use in medical procedures. This in turn raises the issue of an increasing number of samples entering long-term storage without the possibility to check that thermal damage has not occurred during storage and before eventual use. A recently published paper by Professor Heiko Zimmermann and his colleagues from Saarland University's Biophysics and Cryotechnology department lays out a possible framework to address this issue [1]. It describes a powerful new technique that offers the ability to not only verify the absence of physical and chemical change due to devitrification inside the sealed sample, but also automate periodic, non-invasive monitoring of entire biobank samples.

## Biobanks and Cryopreservation

Biobanks rely on the fact that aqueous samples are considered to be stably cryopreserved upon cooling to below  $-137^{\circ}\text{C}$ , as this is the glass transition temperature ( $T_g$ ) of amorphous water. Chemical and biological activity, and diffusion also virtually stop below this temperature.

Ice crystal formation does not occur below  $T_g$ , which is particularly significant with respect to vitrified samples that have been solidified in a metastable, amorphous (glassy) state by sudden cooling. If ice forms in vitrified samples due to transient infringing of the  $T_g$  (devitrification), ramification of the crystals will lead almost inevitably to the loss of the complete sample. Transient warming incidents sufficient to cause ice crystal formation are possible in biobanking practice, for example when moving single specimens or entire sample collections. But, the potentially ruinous effects

on the sample of an interruption in the cold chain are not currently detectable before rewarming, i.e. ahead of specimen use. Until now, technical solutions for monitoring the integrity of the sample in situ have not been available and there has been no established technique for retrospective proof of physical and chemical changes inside the sealed sample.

## Optical monitoring

The team from Saarland University has demonstrated a powerful, Raman-scattering based technique for non-invasively monitoring and investigating cryopreserved samples. In particular, they have confirmed unambiguously the detection of ice crystals in vitreous samples in situ at temperatures below  $-120^{\circ}\text{C}$ .

They focused on the OH-stretching band to investigate whether the sample water is amorphous or crystalline. Conditions in cryogenic storage and typical slow freezing conditions were mimicked using a cooling stage capable of a rate of  $-1\text{K} / \text{min}$ . At the heart of the Raman detection system is a fibre-borne Shamrock 303i imaging spectrograph from Andor coupled to an iDus back-illuminated deep-depletion ('BRDD') CCD camera in order to access the longer illumination wavelength if cellulat autofluorescence became an issue. According to Professor Zimmermann, a bespoke Labview-based software was developed to allow data capture, export and processing.

Zimmerman's team created chemical maps of the samples using confocal Raman microscopy. Each pixel of the image contains an entire Raman spectrum, and images of arbitrary spectral channels can be generated to display isolated, useful molecular vibrations. In this way, Raman microscopy can measure and map the concentration as well as the chemical state of the main constituents of a sample. Figure 1 is a confocal Raman micrograph of the phase texture of frozen biobanking media at  $-50^{\circ}\text{C}$ . Ice crystals are visible as dark areas separated by fluid channels enriched in DMSO (green)

with hydrohalite, a crystalline rock salt hydrate only stable at sub-zero temperatures, visible as red.

To resemble typical slow freezing conditions, the team cooled a single suspended human mesenchymal stem cell (hMSC) down to  $-120^{\circ}\text{C}$  at a rate of  $-1\text{K} / \text{min}$  in a PBS solution containing 10% DMSO and collected the Raman images. Then, in order to prove the concept of monitoring recrystallization of vitrified samples during cold storage and the possibility of thermal damage during routine biobanking operations, the team mimicked a measured typical temperature profile of a sample vial while a neighbouring vial was withdrawn from the cryocontainer. They started the monitoring process at  $-141^{\circ}\text{C}$  and heated the sample at a rate of  $2\text{K} / \text{min}$ . Until a temperature of  $-127^{\circ}\text{C}$ , the spectra show no significant changes but crystallization onset was detected at approx.  $-127^{\circ}\text{C}$  and completed at approx.  $-122^{\circ}\text{C}$ . Figure 2 is a contour diagram showing the emergence of a characteristic 'ice band' due to devitrification upon rewarming a sample beyond the glass transition temperature at approx.  $-125^{\circ}\text{C}$ . Furthermore, the 'ice band' was reproducibly detected on crystallization of samples of various compositions, including cell suspensions. In this way, Zimmermann and his co-workers have demonstrated how the fatal effect of devitrification – ice formation in vitreous samples – can be unambiguously detected by Raman spectroscopy below  $-120^{\circ}\text{C}$ .

## The potential in Biobanking

Raman probe screening of cryopreserved samples could be the first stage in establishing a recognised technique for retrospective proof of the absence of physical and chemical changes inside the sealed sample due to devitrification. Furthermore, this technique allows a differentiation between cryoprotective agents (CPAs) as well as freezing protocols, such as vitrification or slow freezing. Moreover, in principle the technique is capable of detecting any other chemical change in samples and has the potential to be a powerful method for contactless monitoring of the status of cryopreserved samples during storage.

Implementation of the concept could lead the way to automated monitoring of samples under cryogenic storage in the future, although storage technology would need to evolve to allow transport of samples to an optical interface inside the cryo-tank. It is possible that this degree of complexity and cost will only be considered for very valuable samples.

In the short term, however, the authors have shown that it would be possible to take a fingerprint spectrum of every freshly preserved sample and use it as a reference to periodically confirm sample integrity during storage and upon eventual release. The research has also shown that their confocal setup and the present fibre probe already allow measurements through turbid container walls, such as Teflon straws, and the team is working

on the development of a multispot confocal probe for workbench applications.

They suggest that biobanking practice incorporates the pre- and post-storage sample characterisation in cryogenic temperature workbenches to check for chemical changes during the conservation and for ice formation in vitrified samples. A quality assessment for sample transportation can also be performed this way. They also suggest that Raman spectroscopy could be used to develop catalogue references for the quality management of cryopreserved samples and that comparison of existing samples with catalogued spectra may enable retrospective sample analysis.

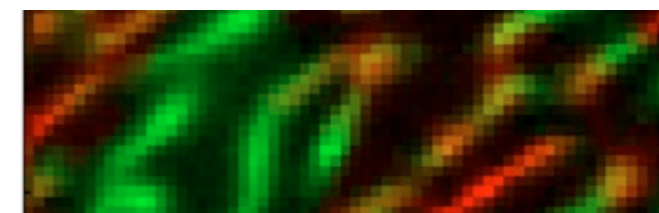


Figure 1: A confocal Raman micrograph ( $65 \times 65 \mu\text{m}^2$ , colour-coded for chemical compounds) of the phase texture of frozen biobanking media at  $-50^{\circ}\text{C}$ . Ice crystals are visible as dark areas separated by fluid channel enriched in DMSO (a well-known cryoprotective agent) highlighted in green. The red structures were identified as hydrohalite – a crystalline rock salt hydrate only stable at sub-zero temperatures.

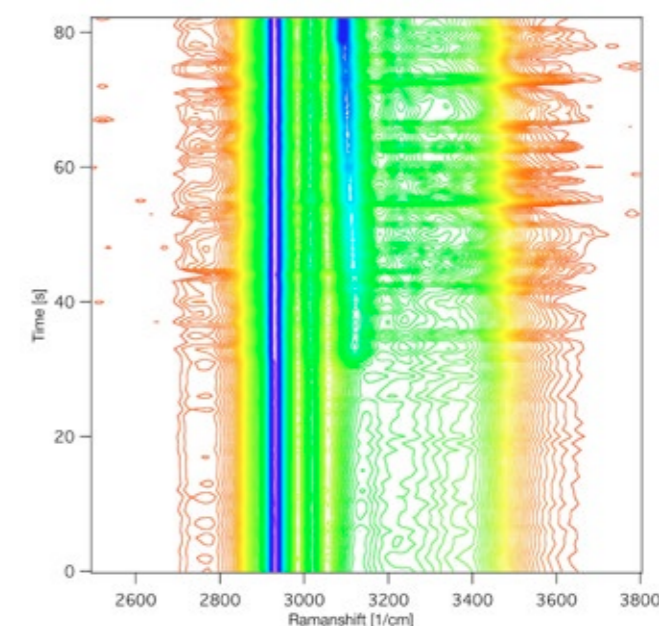


Figure 2: A contour diagram showing the emergence of the ice band ( $3120\text{ cm}^{-1}$ ) due to devitrification upon rewarming of the sample beyond the glass transition temperature at about  $-125^{\circ}\text{C}$ .  $T = 0\text{ s}$  corresponds to a temperature of  $-141^{\circ}\text{C}$ , while the heating gradient was  $2\text{K} / \text{min}$ .

## References

- [1] Daniel Dorr, Frank Stracke, and Heiko Zimmermann, Noninvasive Quality Control of Cryopreserved Samples. Biopreservation and Biobanking Vol. 10, No. 6, p529-531 (2012)

# Probing Molecular Structure with Low Frequency Raman Spectroscopy

James Carriere  
Ondax Inc. | [www.ondax.com](http://www.ondax.com)

Raman spectroscopy has become an extremely valuable tool for measuring and identifying chemical composition and molecular structures. Traditional applications of Raman spectroscopy focus on Stokes signals, 200 - 4000  $\text{cm}^{-1}$  away from the excitation laser line. Access to the low frequency Raman region ( $<10 \text{ cm}^{-1}$  - 200  $\text{cm}^{-1}$ ) has traditionally been reserved for specialized instruments due to the limitations of optical components typically used in filter based Raman spectrographs.

## Introduction

The importance of Raman spectroscopy as an analytical tool is based on the ability to probe the unique vibrational and rotational modes of molecules. The frequencies of the transitions probed by Raman typically range from 200 - 4000  $\text{cm}^{-1}$ .

The low frequency Raman region ( $<10 \text{ cm}^{-1}$  - 200  $\text{cm}^{-1}$ ) probes the same low energy vibrational and rotational modes of molecular structures as terahertz spectroscopy (300 GHz - 6 THz). Many materials exhibit strong uniquely identifiable ultra-low frequency Raman spectra as characteristics of their low energy vibrational and rotational modes. Examples of some applications which take advantage of low frequency Raman signals are:

- Discrimination of compounds with polymorphic structures, such as active pharmaceutical ingredients and organic semiconductors [1].
- Semiconductor analysis: advanced semiconductor devices have strong signals in the low frequency region [2] from folded acoustic and shear modes of multilayer super-lattice structures.
- Analysis of low energy vibrational modes of large, complex molecules such as compounds that contain heavy atoms or radioactive isotopes [3].

- Measurement of rotational and vibrational temperatures in optical pumped gas cells [4].

Obtaining these low frequency signals ( $<200 \text{ cm}^{-1}$ ) has previously been difficult and costly due to the limitations of available filters for blocking the intense Rayleigh scattered laser light.

## Experiment Setup

A low frequency Raman spectrograph capable of measuring signals  $<10 \text{ cm}^{-1}$  from the laser line was built and used to measure L-Cystine (Figure 1). The system, which is based on Ondax SureBlock ultra-narrow-band filters and an Andor spectrograph, is much more compact, economical and easier to use than the triple stage spectrographs that are typically used to access these low frequency transitions. The high performance of the Ondax SureBlock filters enable access to the low-frequency region of Raman spectra with a conventional visible or NIR laser using only a low stray-light, high dispersion single stage spectrograph. The combined system offers the advantage of being able to simultaneously measure both the low frequency Stokes and anti-Stokes signals without sacrificing the ability to measure traditional Raman shifts of 2000  $\text{cm}^{-1}$  or more.

The Low Frequency Raman Spectrograph (Figure 2) consisted of either a 532 nm or 785 nm wavelength

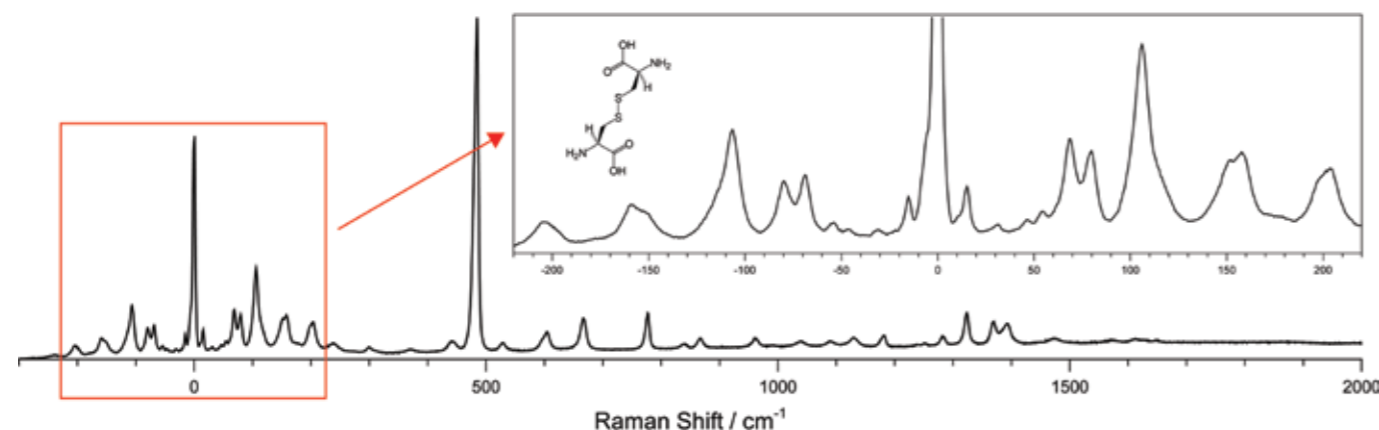


Figure 1: The low frequency Raman spectra of L-cystine showing both the low frequency Stokes and anti-Stokes region as well as the “fingerprint” region transitions. 532 nm excitation wavelength was used and the spectra was collected for a total integration time of 120 seconds using a Shamrock 303i equipped with a 1800 l/mm groove density grating and an iDus DU420A-OE detector.

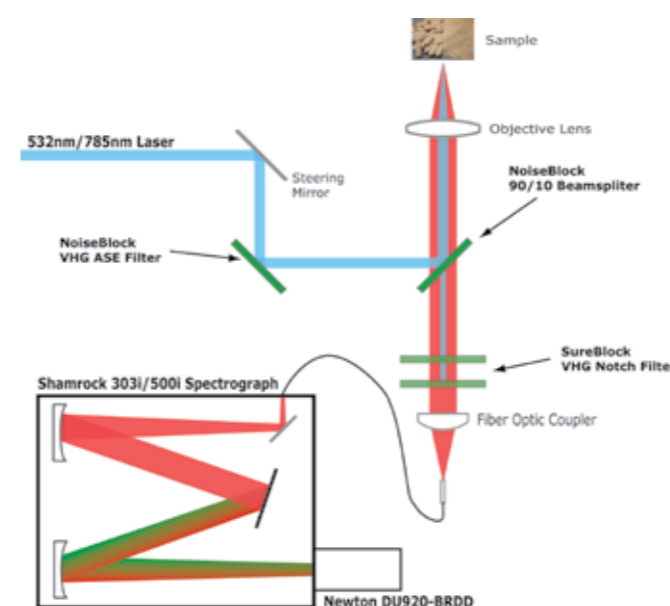


Figure 2: Diagram of the Low Frequency Raman Spectrograph. Collimated light from either the 785 nm or 532 nm excitation source was focused onto the sample after filtering and redirected by an ASE suppression filter and matching 90/10 beamsplitter (Ondax Incorporated). The resultant Raman signal was collected by a focusing objective and fibre coupled to either an Andor Shamrock 303i or Shamrock 500i after the Rayleigh scatter was removed by two Ondax SureBlock ultra narrow-band notch filters. The dispersed light was detected by either a Newton DU920P-BRDD or an iDus DU420A-OE.

stabilized laser with the ASE removed using a narrow-band ASE suppression filter. A matching 90/10 beamsplitter redirected the beam towards an objective lens focused onto the sample of interest. The backscattered signal was re-collimated by the objective lens and in the return path, the 90/10 beamsplitter transmitted the Raman signal while reflecting 90% of the Rayleigh scattered light. Two Ondax SureBlock ultra narrow-band notch filters, each having optical density (O.D.)  $> 4$ , were used to block the remaining Rayleigh scattered light for an estimated total optical density of  $\sim 9$ . The filtered Raman signal was then fiber coupled to a spectrograph (Shamrock 303i or 500i) and onto either a back-illuminated deep depletion Newton CCD detector (DU920P-BRDD) or an open-electrode iDus CCD detector (DU420A-OE). Typical integration times of 60 seconds were used to capture the Raman spectra.

To illustrate the ability to distinguish between different polymorphic structures, three different forms of carbamazepine (a common drug used as an anti-convulsant) were measured with the low frequency Raman spectrometer (Figure 3). The region from 20 - 60  $\text{cm}^{-1}$  shows a clear distinction between the three different forms with virtually no overlap of the signals even though all three forms have identical chemical compositions with few distinguishing features in the “fingerprint” region of the Raman spectra. This and similar low-frequency Raman measurements could be used in the development and production of pharmaceuticals and the synthesis of other chemical compounds to not only identify and verify the purity of a preparation but to also ensure the proper formulation has been prepared to FDA standards.

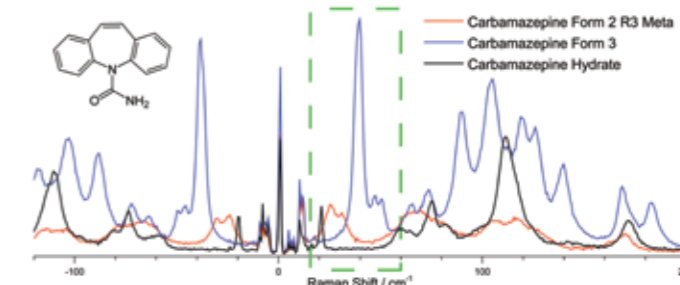


Figure 3: The 20-40  $\text{cm}^{-1}$  region of the low frequency Raman spectra of Carbamazepine can be used to distinguish its various isoforms, a critical function in the manufacturing of the drug. Spectra were taken using the low frequency Raman spectrograph, the excitation wavelength was 785 nm and the spectra was collected with total integration time of 60 sec using a Shamrock 500i equipped with a 1200 l/mm groove density grating and an iDus DU420A-OE detector.

## References

- [1] Ranzieri, P., Girlando, A., Tavazzi, S., Campione, M., Raimondo, L., Bilotti, I., Brillante, A., Della Valle, R. G. and Venuti, E., Polymorphism and Phonon Dynamics of  $\alpha$ -Quaterthiophene. *ChemPhysChem*, Vol 10, p657–663 (2009)
- [2] Tan, P.H., Han, W.P., Zhao, W.J., Wu, Z.H., Chang, K., Wang, H., Wang, Y.F., Bonini, N., Marzari, N., Savini, G., Lombardo, A. and Ferrari, A.C., The Shear Mode of Multi-Layer Graphene. *arXiv:1106.1146v1 [cond-mat.mes-hall]* (2011)
- [3] Pakhomov, P., Khizhnyak, S., Galitsyn, V., Rogova, E., Hartmann, B. and Tshmel, A., Application of the Low Frequency Raman Spectroscopy for Studying Ultra-High Molecular Weight Polyethylenes. *Macromolecular Symposia*, Vol 305, p63–72 (2011)
- [4] Walter, D.K., Griffith, W.M. and Happer, W., Energy Transport in High-Density Spin-Exchange Optical Pumping Cells. *Phys. Rev. Lett.*, Vol 86, p3264-3267 (2001)

# Spectral characteristics of an integrated Type-I parametric down-conversion source in Ti:PPLN waveguides

S. Krapick, H. Herrmann, V. Quiring, B. Brecht, H. Suche and Ch. Silberhorn  
Integrated Quantum Optics Group, Department of Physics, University of Paderborn, Germany

In recent research on quantum communication, parametric down-conversion (PDC) in  $\chi^{(2)}$ -nonlinear crystals plays a major role for the generation of photon pairs (see e.g. [1], [2], [3]). In particular, the addressing of atomic transitions for quantum memory applications [4], [5] requires a precise knowledge of the spectral emission characteristics of PDC sources. New generation of photon pair sources relies on increased functionalities integration on one chip with sophisticated wave guiding structures providing nonlinear conversion efficiencies, which are several orders of magnitude higher than those of any bulk crystal [6].

## Introduction

Z-cut Lithium Niobate (LN) is a well-understood material with high nonlinearity properties. It can allow the fabrication of high quality guides which can confine wave propagation over several centimeters, whereas high pump intensity in bulk crystals can only be achieved over much shorter distance.

In this work, a Research team at the University of Paderborn spectrally characterized a nondegenerate Type-I PDC source in Titanium-indiffused periodically poled Lithium Niobate (Ti:PPLN), where a pump photon at 532 nm polarized along the extraordinary crystal axis decays into two photons with the same polarization at around 800 and 1575 nm respectively.

Figure 1 shows the schematic of the source. It consists of a Ti:PPLN waveguide, which was periodically poled with a periodicity of around 6.8  $\mu\text{m}$  to achieve so-called quasi-phases-matching.

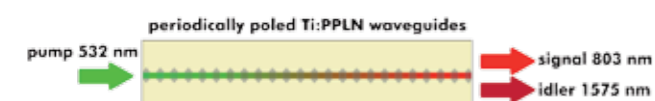


Figure 1: Schematic of the Ti:PPLN photon-pair source

## Parametric down-conversion

Parametric down-conversion is a three-wave-mixing process, where pump photons of a specific energy, represented by their wavelength  $\lambda_p$ , can couple to a vacuum quantum state and decay into two daughter photons, commonly labeled signal (s) and idler (i). For this process, energy conservation has to be fulfilled:

$$\frac{1}{\lambda_p} = \frac{1}{\lambda_s} + \frac{1}{\lambda_i} \quad [i]$$

Furthermore the conservation of momentum must hold:

$$\vec{k}_p = \vec{k}_s + \vec{k}_i \quad [ii]$$

where the different  $\vec{k}$  represent the wave vectors of the respective photons. This equation is usually called phase-matching condition. In bulk  $\chi^{(2)}$ -nonlinear and birefringent optical materials, an angular degree of freedom is given with respect to the phase-matching condition, so that specific combinations of signal and idler wavelengths can be achieved by tuning this angle.

In contrast, waveguides in nonlinear materials can confine light over longer distances due to total reflection of light at the waveguide boundaries, implying a restriction to only one translation degree of freedom, i.e. the propagation direction of the interacting photons. This also implies the limitation to only one translatory degree of freedom, namely the propagation direction of the interacting photons. The wave vectors can be replaced by scalars of effective wave numbers for the individual guided mode:

$$k = \frac{2\pi}{\lambda} n_{eff}, \quad [iii]$$

where  $\lambda$  represents the photon wavelength and  $n_{eff}$  is the effective refractive index. Due to chromatic dispersion, a phase-mismatch occurs in waveguided PDC processes:

$$k_p - k_s - k_i = \Delta k. \quad [iv]$$

Here the additional parameter  $\Delta k$  expresses the phase mismatch in terms of additional wave number. To compensate for this, a common technique called periodically poling is employed. The spontaneous polarization inversion in the crystallographic medium introduces an additional rating vector, which modifies the phase-matching condition of equation (ii). The required poling period  $\Lambda_G$  is given by:

$$\Delta k = \frac{2\pi \cdot m}{\Lambda_G}, \quad [v]$$

where  $m$  is an odd integer representing the order of the quasi-phases-matching. Together with the conservation

of energy given by Equation (i), the conservation of momentum defines the possible wavelength combinations for a given poling period in waveguide-based PDC processes. For a given pump wavelength and poling period, the wavelength combination of signal and idler can be determined. Tuning those wavelengths can be accomplished by varying the temperature of the device.

This property is linked to the temperature dependence of the effective refractive indices. For applications requiring stable PDC sources, it is therefore important to understand and characterize the spectral shift with device temperature.

## Waveguide Technology

For these experiments, waveguides with a fixed width of 7  $\mu\text{m}$  were manufactured. The polishing periods were varied between 6.71 and 6.91  $\mu\text{m}$  across the device width. The waveguides were fabricated by Titanium-indiffusion at 1060°C over 8.5 hours. To achieve the best possible coupling of light into and out of the waveguides, the end-facets were polished perpendicularly to the propagation direction. To improve the overall conversion efficiency of the device, Krapick's team developed and deposited dielectric coatings (EFC) for optimum incoupling of the pump wavelength. The best possible outcoupling of signal and idler wavelengths, including the reflection of the pump, was achieved by a 16-layer coating at the waveguide output.

## Experimental Setup

The setup used for the nonlinear optical characterization is shown in Figure 2.

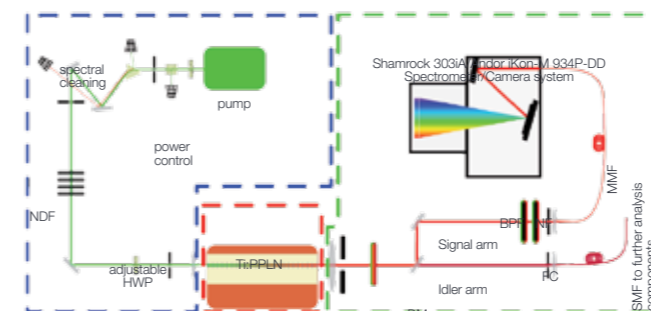


Figure 2: Experimental setup for spectral PDC measurements; NDF: neutral density filters, BL: beam blocker, HWP: half-wave plate, RG715: customized absorptive filter, DM: dichroic mirror, NF: needle filter, BPF: band-pass filter, FC: fiber coupling stages, MMF: multi-mode fiber. SMF: single-mode fiber

A prism-based beam cleaning ensures that only the pump wavelength is launched into the device, and variable attenuators in combination with neutral density filters are used to control the optical pump power. The TM polarization is set by an additional half-waveplate positioned before the AR-coated coupling lens.

The sample alignment setup consists of a home-built high-precision five-axis stage, while the temperature can be changed or stabilized at sufficiently high levels

to prevent so called photorefractive damage ( $T > 140^\circ\text{C}$ ), which is the light-induced, highly dynamic change of refractive indices mediated by the nonlinear electro-optic effect.

The team chose a flexible free-space configuration including several (partially home-made) spectral filters and absorbers for high transmission of the signal and idler beams.

A dichroic mirror splits the PDC output into signal and idler arms, with the signal arm being coupled to a multimode fiber. The PDC spectral characterization is done by an Andor iKon-M DU934P-BR-DD CCD detector coupled to a Shamrock SR303i-A-SIL with silver-coated optics for enhanced efficiency in the near infrared, and an XY adjustable fiber. The Shamrock spectrograph triple grating turret and entrance slit were adjusted remotely through Andor Solis software.

A 1200 l/mm grating blazed at 500 nm was used in conjunction with a 10  $\mu\text{m}$  wide slit to achieve the highest possible resolution. The CCD acquisition mode was set to full vertical binning operation and kinetic series. A readout speed of 50 kHz and a pre-amplifier of 4 were chosen to obtain the best signal to noise ratio performance. The exposure time was chosen to be 0.025 s.

## Results and Discussion

The nonlinear characteristics of the PDC source have been determined by measuring the spectral behavior with changing device temperature or with different poling periods. Figure 3 (overleaf) shows the coarse and fine wavelength tunability associated with poling period and temperature variation respectively. A strong dependence of the PDC signal emission on the poling period and the position on the device was identified. The higher central peaks indicate stronger nonlinear interaction efficiency in the central parts of the PDC device. The team explained this phenomena by the presence of a more homogeneous periodic poling pattern in this section, while in the edge regions the poling slightly suffers from so called over- or underpoling. This reduces the effective interaction length of the PDC process.

Figure 3 shows the possibility for precise control of the generated wavelengths by tuning the device temperature. The Andor detection system provided the high sensitivity necessary for these measurements, while also exhibiting negligible optical etaloning. The graphs in Figures 3 and 4 show no significant impact on the spectral profile of the optical interferences within the sensor's Fabry-Pérot interferometer-like structure. For the high pre-amplifier gain chosen, the base level was around 300 counts.

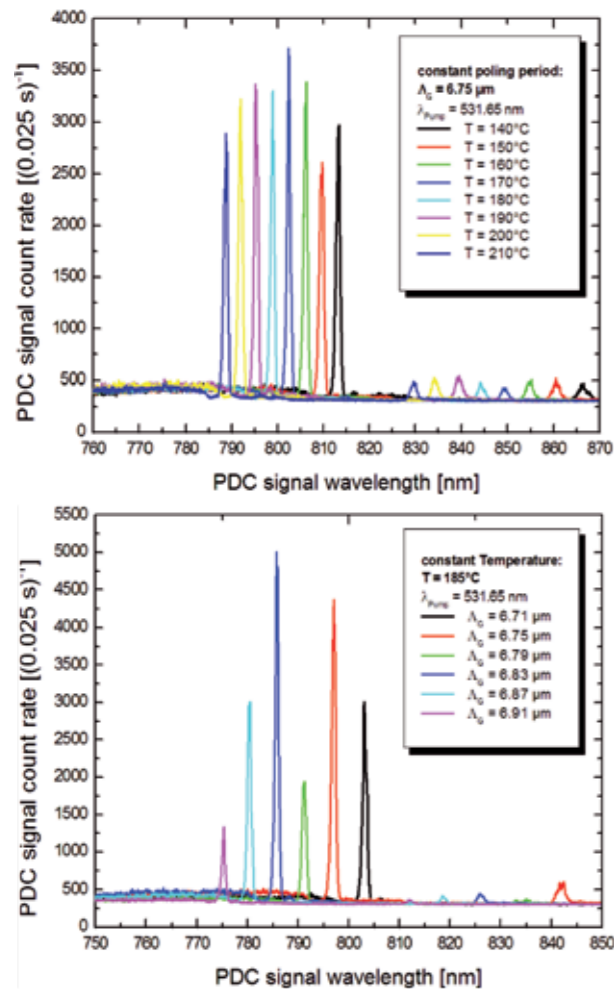


Figure 3: Tunability of the PDC signal wavelength with the crystal's poling period (top) and temperature (bottom)

It should be noted that one spectrum consists of only one sidepeak, indicating a higher order spatial waveguide mode excitation around 45 nm shifted to longer wavelengths. This shows excellent waveguide homogeneity and good coupling of the pump light to the fundamental spatial waveguide mode.

In preparation of later experiments, a dielectric needle filter was implemented to the signal arm. With this, the spectral characteristics of the PDC source in the Silicon detection band exhibited no additional photon signal exceeding 0.6% of the maximum PDC signal level.

The needle filter has a FWHM bandwidth of <math><0.5\text{ nm}</math> and a maximum classical transmission of  $T_{\text{NF,S}}=0.78$  as shown in Figure 4 and its inset. The large wavelength range shown in the inset graph was obtained with the software-controlled 'step and glue' mode of the spectrograph. This allowed broadband spectral acquisition at higher resolution.

## Conclusion

The team at University of Paderborn spectrally characterized a waveguide-based type-I PDC source in Titanium-indiffused waveguides in periodically poled Lithium Niobate with a single-photon sensitive high-

resolution spectrograph and was able to verify its excellent performance with respect to sample homogeneity and tunability.

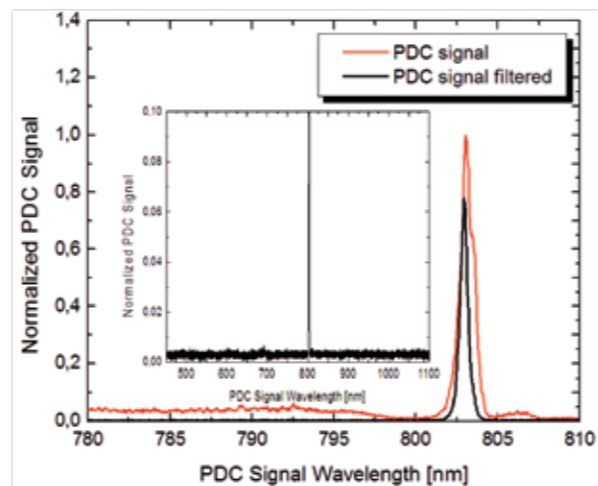


Figure 4: Unfiltered (red) and needle-filtered PDC signal (black), inset: background spectral characteristics

## References

- [1] A. Martin, O. Alibert, M. P. De Micheli, D. B. Ostrowsky, and S. Tanzilli. A quantum relay chip based on telecommunication integrated optics technology. *New Journal of Physics*, 14(2):025002 (2012)
- [2] A. Christ, C. Lupo, K. Laiho, A. Eckstein, K. N. Cassemiro, and C. Silberhorn. Multimode ultrafast broadband information coding: State generation, characterization and loss evaluation. In *CLEO/ Europe and EQEC 2011 Conference Digest*, page EA12, Optical Society of America (2011)
- [3] N. Sangouard, B. Sanguinetti, N. Curtz, N. Gisin, R. Thew, and H. Zbinden. Faithful entanglement swapping based on sum-frequency generation. *Phys. Rev. Lett.*, 106(12):120403 (2011)
- [4] C. Clausen, I. Usmani, F. Bussires, N. Sangouard, M. Afzelius, H. de Riedmatten, and N. Gisin. Quantum storage of photonic entanglement in a crystal. *Nature*, 469:508-511 (2011)
- [5] E. Saglamyurek, N. Sinclair, J. Jin, J. A. Slater, D. Oblak, F. Bussires, M. George, R. Ricken, W. Sohler, and W. Tittel. Broadband waveguide quantum memory for entangled photons. *Nature*, 469:512-515 (2011)
- [6] M. Fiorentino, S. M. Spillane, R. G. Beausoleil, T. D. Roberts, P. Battle, and M. W. Munro. Spontaneous parametric downconversion in periodically poled KTP waveguides and bulk crystals. *Opt. Express*, 15(12):7479-7488 (2007)

## For more information ...



Search for the technical note entitled 'Optical Etaloning in Charge Coupled Devices (CCDs)' at [andor.com/learning](http://andor.com/learning)

# Three-Dimensional Plasmonic Nanoclusters

Urban AS, Shen X, Wang Y, Large N, Wang H, Knight MW, Nordlander P, Chen H and Halas NJ  
Laboratory for Nanophotonics, Rice University, Houston, Texas, United States

Assembling nanoparticles into well-defined structures is an important way to create and tailor the optical properties of materials. These optical properties of subwavelength metallic structures arise from their ability to support surface plasmons, oscillations of the delocalized electrons in metals that couple with the electromagnetic field.

## Introduction

A universal characteristic of these structures is their exquisite correlation between structural geometry and optical properties, which has provided new approaches to the control and manipulation of light, particularly in the visible and near-infrared regions of the spectrum [1]. [2].

This has made it possible to engineer electric and magnetic responses over this wavelength range, enabling the construction of metamaterials with a negative refractive index at these wavelengths, [3], [4] along with a host of artificial media that manipulate light in ways that defeat natural materials [5], [6], [7].

Most advances in metamaterials research to date have been based on structures fabricated in two-dimensional planar geometries. Although 3-D nanocluster assembly has been reported, [8], [9], [10], [11], [12] cluster stability and robustness has been limited, with disintegration or deformation apparent if removed from the solution or substrate where they were formed or through contact with other solvents or solutions. [9], [13], [14] Aging effects, such as contraction of DNA, may also lead to radical changes in morphology.

In this work, the team at Rice University shows an efficient method for fabricating highly regular, stable 3-D plasmonic nanoclusters of noble metals by encapsulation within a small polymer sphere that stabilizes their geometry and protects them against a wide range of solvents and solutions. The structural integrity of these clusters allowed an examination of how the optical properties of individual 3-D clusters relate to nanoparticle number, geometry, and orientation of the cluster. Some of the clusters, such as tetrahedra and icosahedra, could serve as the optical kernels for metafluids, imparting metamaterial optical properties into disordered media such as liquids, glasses, or plastics, free from the requirement of nanostructure orientation.

## Fabricating 3-D Nanoclusters

Obtaining small clusters of close packed nanoparticles is quite challenging; the constituent nanoparticles need to be mobile enough to achieve a minimal energy state, yet stable enough to prevent dissociation and aggregation during their isolation and subsequent study.

The Rice team incubated citrate-stabilised 15 nm gold nanoparticles with thiol-terminated polystyrene (PS115-SH) and PS17-b-PAA83 in DMF. The swelling of the long polystyrene chains allows the nanoparticles to maximize their packing within the cluster. Aggregation was induced by adding water to remove the DMF and clusters were directly isolated by centrifugation before characterisation by transmission electron microscopy (TEM) or scanning electron microscopy (SEM).

This fabrication process resulted in a variety of highly regular 3-D clusters containing predominantly 3 - 25 nanoparticles, with an interparticle spacing of nominally 10 nm. In small clusters of three to six particles, the structures formed were triangular, tetrahedral, trigonal bipyramidal, and octahedral, respectively. For larger clusters of 7 to 20 particles, the structures follow an essentially icosahedral growth scheme, with the structures either assembling en route to, or growing onto, an icosahedral cluster. Interestingly, the yield of icosahedral (N = 13) and double-icosahedral clusters (N = 19) is significantly larger than the yield of even slightly differently sized clusters and is directly reminiscent of "magic number" atomic clusters.

## Characterisation of the Nanoclusters

Dark-field scattering spectra of specific individual monomers, dimers, trimers, and tetrahedra of the nanoclusters were acquired. ITO-coated float glass substrates were patterned with gold/titanium finder grids comprising 100 x 100 μm squares to repeatedly locate individual nanoparticles in both dark field and scanning electron microscopes. Following dilution to enable imaging of single clusters, 1.5 μL of solution was drop-cast on each sample and allowed to dry.

The substrates were illuminated with a quartz halogen aluminium reflector and imaged in an oil-immersion, transmission dark field microscope with a 40x 0.6NA objective (Olympus Corporation). Spectral analysis was provided by a hyperspectral system, comprising a diffraction grating spectrophotometer with automated sample stage (CytoViva technology) with a back illuminated, deep depletion CCD (iKon-M DU934P-BR-DD, Andor Technology). The camera cooling was maintained at -80°C and a total of 251 image slices were acquired at 4 slices per second, with nanoparticle spectra automatically generated through specially-written software from Igor Pro (WaveMetrics).

## Results and Discussion

A dark-field scattering spectrum for each individual nanocluster was recorded (Figure 1a, b) and compared with finite element method calculations of the theoretical scattering spectra (Figure 1d). Each individual nanocluster was also imaged by scanning electron microscopy (Figure 1c).

Among these small 3-D clusters, three primary characteristics emerged.

1. The 3-D spatial orientation of the dimer and trimer clusters has a dominant and dramatic influence on the shape of their respective spectra.
2. In contrast to the dimers and trimers, the tetrahedral clusters appeared to have remarkably isotropic optical properties.
3. The localized surface plasmon resonance of the monomer was strongly red-shifted and broadened relative to Mie theory for a polymer-encapsulated monomer of equivalent size, geometry, and orientation. This is a critical observation, since a quantitative understanding of the monomer resonance is crucial to our analysis of the optical responses of the substantially more complex multiparticle clusters.

Finite element method (FEM) calculations using the geometric parameters of the SEM images were adjusted in respect of shape, size, substrate and symmetry to account for experimental observations. The observed spectral red-shift of the monomer was shown to be consistent with the presence of a thin silver oxide shell around the nanoparticles. However, the presence of an Ag oxide shell accounted for only 20% of the experimentally observed broadening of the monomer plasmon resonance. An additional contribution to the broadening is the diffusion of silver ions and impurities into the surrounding PS-PAA polymer during the cluster formation process. Indeed, a close agreement with the experimental scattering spectra for the monomer resulted when the PS-PAA polymer was modelled as a lossy medium with  $\tilde{n} = n + ik$ , where  $n = 1.6$  and  $k$  is in the range 0.04 - 0.38. Using this observation as a starting point, the team obtained excellent agreement between the calculated and measured scattering spectra for the clusters shown in Figure 1b-d.

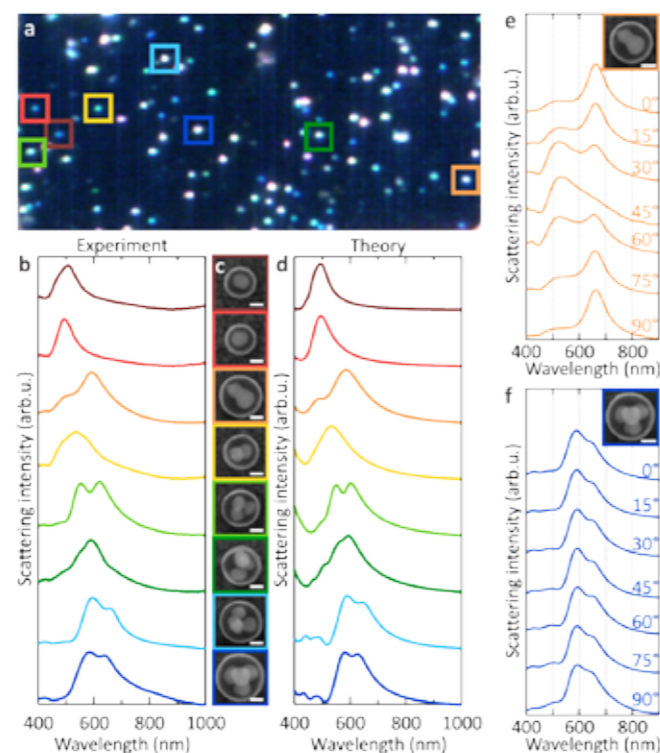


Figure 1: Optical properties of small ( $N \leq 4$ ) nanoclusters. (a) Dark-field scattering hyperspectral image of nanoclusters performed over  $100 \times 100 \mu\text{m}$  squares, (b) Small ( $N \leq 4$ ) silver nanoclusters dark-field scattering spectra. Corresponding SEM images are shown in c. (d) Finite element method calculations of the scattering spectra of the individual nanoclusters (e) Polarization-dependent scattering spectra of the dimers (f) Polarization-dependent scattering spectra of the tetrahedron. Scale bars correspond to 50 nm.

The clusters, while supported on a substrate for the purposes of optical characterisation, retain a random, 3-D, out-of-plane orientation due to their round polymer capsule. This 3-D orientation induces profound changes in the observed optical properties and is shown dramatically in the scattering spectrum of the dimer and trimer clusters, where any change in orientation of the cluster with respect to incident light polarization reveals large spectral shifts and the appearance of additional modes for specific orientations. Extensive angle-dependent calculations, incorporating slight asymmetries due to nanoparticle position and shape within the cluster, were needed to obtain this level of quantitative agreement, even for the simplest cluster geometries. The polarization dependence of the dimer and tetrahedral clusters was examined in greater detail by inserting a linear polariser into the emission path of the microscope and acquiring polarisation-dependent scattering spectra.

The highly orientation-dependent scattering spectrum of the dimer, comprised of linear combinations of transverse and longitudinal plasmon modes, could be clearly observed for this randomly oriented case (Figure 1e). In contrast, the scattering spectrum of the tetrahedron is nearly isotropic (Figure 1f). This observed isotropy provides direct evidence that a plasmonic tetrahedron does indeed behave like an isotropic "metamolecule": such clusters can be dispersed in a

liquid and result in a metafluid.

As previously mentioned, determining the structure of larger nanoclusters is quite challenging. However, geometrical information can be extracted by comparing their measured optical properties to the calculated optical properties of modelled nanoclusters. To illustrate this possible approach, the Rice team chose a nanocluster which appeared to be an icosahedron in SEM images, another nanocluster with isotropic optical properties (Figure 2a). Indeed, the polarization-dependent scattering spectra of this far more complex cluster vary only weakly with polarization angle (Figure 2b) and are in good agreement with theoretical simulations for a perfect icosahedron (Figure 2c).

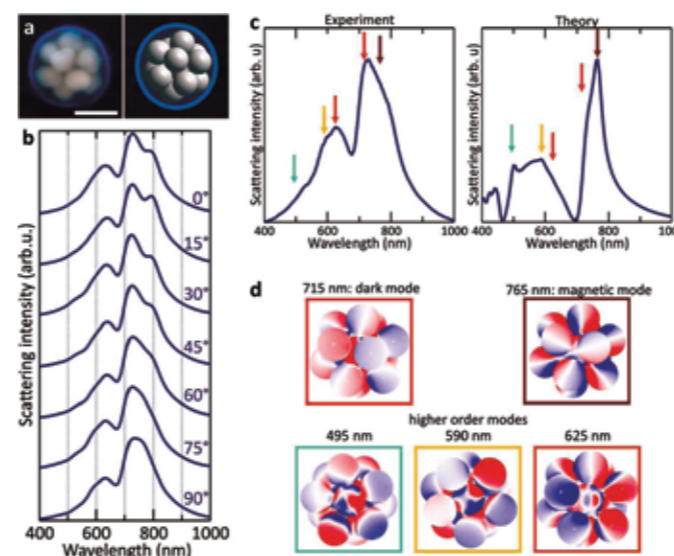


Figure 2: Optical properties of icosahedral clusters. (a) SEM image (left) and 3-D model (right) of an icosahedron (13 NPs). The scale bar corresponds to 100 nm. (b) Polarization-dependent scattering spectra of the icosahedron. (c) Experimental scattering spectra from the FEM calculations. (d) Charge plots of the modes identified in the scattering spectrum of the icosahedron.

Five main localized surface plasmon modes contribute to the calculated spectrum of the icosahedron, as can be seen in the charge plots calculated for each mode (Figure 2d). The two main peaks are associated with a magnetic plasmon mode at 765 nm and a dark plasmon mode at 715 nm. The other three modes, located between 495 and 625 nm, are higher order modes, which can be seen from the calculated charge distributions (Figure 2d). All of these modes show up in the experimental spectrum at approximately the same positions as in the calculations. The observed variations in the relative peak intensities between the experiment and the simulations can be explained by slight structural imperfections in the fabricated structure, mostly arising from variations in shape of the constituent nanoparticles. The team's conclusion from this direct comparison was that this nanocluster is an icosahedron.

## Conclusion

These nanoparticle clusters open up access to a novel breed of optically active materials. The precise way in

which the nanoparticles are arranged, rather than their composition, dictates the optical characteristics through an effect called localized surface plasmon resonance. Clusters with highly orientation-independent optical properties, such as tetrahedra and icosahedra, could enable polarization-independent and non-directional negative index media like fluids, free-form solids and isotropic films.

The universality of the fabrication method could extend the use of plasmonic nanoclusters to other regions of the spectrum, either by incorporating different materials, for example, aluminium for the UV; or spherical core/shell nanoparticles, for example, nanoshells for the IR. They are also compatible with easily applied material coating methods, such as aerosols, and could lead to materials with transparency windows at specific frequencies and with constant ratios and linewidths. They could also enable electromagnetic characteristics not yet achievable in current types of metamaterials as well as new approaches to current technological challenges, such as high-throughput chemical and biological sensing.

Metamaterial engineering provides exciting prospects for future photonics applications, such as, the fabrication of 'super-lenses' that can potentially overcome the diffraction limit associated with traditional lenses.

The structural stability of the nano-bricks at the basis of these metamaterials is critical to ensure consistent and reliable, specific optical properties. For example, knowing that the optical response of an ideal tetrahedron should be virtually independent of cluster orientation is of little use if the 3-D plasmonic nanocluster is unstable. Encapsulating the 3-D nanoclusters in a small polymer sphere stabilizes their geometry, makes them resistant to a wide range of solvents and solutions, and paves the way for the development of novel isotropic metamaterials, such as metafluids.

## References

- [1] Luk'yanchuk, B.; Zheludev, N. I.; Maier, S. A.; Halas, N. J.; Nordlander, P.; Giessen, H.; Chong, C. T. *Nat. Mater.* 9 (9), p707-715 (2010)
- [2] Ni, X. J.; Emani, N. K.; Kildishev, A. V.; Boltasseva, A.; Shalaev, V. M. *Science*, 335 (6067), p427 (2012)
- [3] Kante, B.; Park, Y. S.; O'Brien, K.; Shuldman, D.; Lanzillotti-Kimura, N. D.; Wong, Z. J.; Yin, X. B.; Zhang, X. *Nat. Commun.* 3, p1180 (2012)
- [4] Shalaev, V. M. *Nat. Photonics*, 1 (1), p41-48 (2007)
- [5] Hedayati, M. K.; Faupel, F.; Elbahri, M. *Appl. Phys. A, Mater.* 109 (4), p769-773 (2012)
- [6] Hess, O.; Pendry, J. B.; Maier, S. A.; Oulton, R. F.; Hamm, J. M.; Tsakmakidis, K. L. *Nat. Mater.* 11 (7), p573-584 (2012)

[7] Kuzyk, A.; Schreiber, R.; Fan, Z. Y.; Pardatscher, G.; Roller, E. M.; Hoge, A.; Simmel, F. C.; Govorov, A. O.; Liedl, T. *Nature*, 483 (7389), p311-314 (2012)

[8] Liu, N.; Hentschel, M.; Weiss, T.; Alivisatos, A. P.; Giessen, H. *Science*, 332 (6036), p1407-1410 (2011)

[9] Barrow, S. J.; Wei, X.; Baldauf, J. S.; Funston, A. M.; Mulvaney, P. *Nat. Commun.*, 3, 1275 (2012)

[10] Schade, N. B.; Holmes-Cerfon, M. C.; Chen, E. R.; Aronson, D.; Collins, J. W.; Fan, J. A.; Capasso, F.; Manoharan, V. N. *Phys. Rev. Lett.*, 110, 148303 (2013)

[11] Hentschel, M.; Wu, L.; Schaferling, M.; Bai, P.; Li, E. P.; Giessen, H. *ACS Nano*, 6 (11), p10355-10365 (2012)

[12] Pazos-Perez, N.; Wagner, C. S.; Romo-Herrera, J. M.; Liz-Marzan, L. M.; de Abajo, F. J. G.; Wittmann, A.; Fery, A.; Alvarez-Puebla, R. A. *Angew. Chem., Int. Ed.*, 51 (51), p12688-12693 (2012)

[13] Gellner, M.; Steinigeweg, D.; Ichilmann, S.; Salehi, M.; Schutz, M.; Kompe, K.; Haase, M.; Schlucker, S. *Small*, 7 (24), p3445-3451 (2011)

[14] Bai, F.; Wang, D. S.; Huo, Z. Y.; Chen, W.; Liu, L. P.; Liang, X.; Chen, C.; Wang, X.; Peng, Q.; Li, Y. D. *Angew. Chem., Int. Ed.*, 46 (35), p6650-6653 (2007)

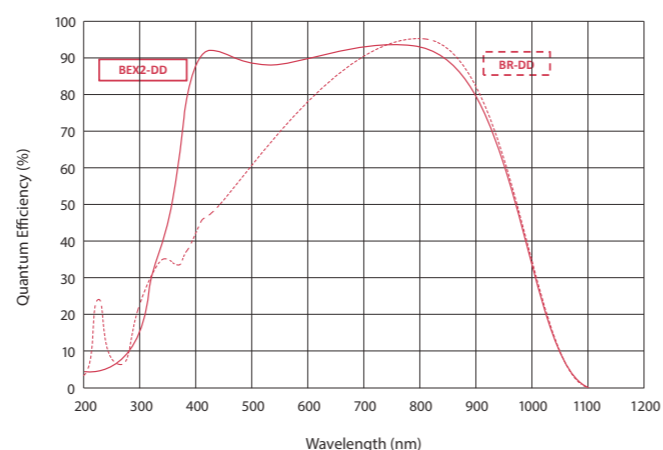
### Optimizing NIR imaging and hyperspectral detection: Back-Illuminated Deep-Depletion iKon CCD platforms

- ✓ Peak QE up to 95% at 850 nm (BR-DD)
- ✓ Dual anti-reflection coating option (BEX2-DD) - enhanced broadband detection
- ✓ Thermo-Electric cooling down to -100°C - negligible dark noise
- ✓ Ultravac™ vacuum technology - maintains quantum efficiency performance year after year
- ✓ Fringe-suppression technology - low optical etaloning in the NIR
- ✓ High resolution 13.5 μm pixel size
- ✓ Integrated shutter - seamless background subtraction
- ✓ 5 MHz readout rate - fast full frame acquisition
- ✓ USB connection

“The Andor iKon-M camera played a key role; the very low dark current due to the advanced thermoelectric cooling combined with high sensitivity over a large wavelength regime allowing us to image even very weakly-scattering nanoparticles to determine their optical properties.”



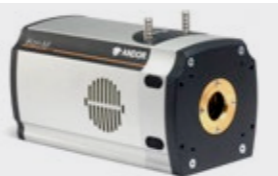
Prof. Peter Nordlander, Professor of Physics and Astronomy, Professor of Electrical and Computer Engineering, Rice University



Quantum Efficiency curves for BR-DD and BEX2-DD sensor types.

For more information ...

Visit [andor.com/ikon](http://andor.com/ikon)



## Quantitative monitoring of biphasic reactions using flow systems by Raman spectroscopy

D. Angelone<sup>(a)</sup>, S. Abdolazadeh<sup>(a)</sup>, J. W. de Boer<sup>(b)</sup>, W. R. Browne<sup>(a)</sup>

(a) Stratingh Institute for Chemistry, University of Groningen, Netherlands, (b) Catexel BV, BioPartner Center Leiden, Netherlands

Biphasic reactions offer tremendous opportunities in industrial chemical syntheses due to the ease at which the phases and hence reagents can be separated, thereby avoiding energy intensive separation processes such as distillations<sup>[1]</sup>. A contemporary challenge presented in the implementation of biphasic reaction conditions is to determine and control the chemistry occurring in each phase, in order to improve manufacturing processes. Inline HPLC techniques for monitoring biphasic reaction have already been developed and demonstrate the potential benefits of inline monitoring in controlling and optimizing reactions<sup>[2, 3]</sup>.

### Introduction

In this contribution, the development of a fully automated system for monitoring changes in the composition of two immiscible phases by Raman spectroscopy using a flow sampling system is presented. This Raman/Flow system can acquire and distinguish Raman spectra of the phases present in an emulsified reaction mixture and offers a key advantage in the real-time information it can deliver. It takes advantage of the new generation of low dark current deep-depletion (LDC-DD) CCD technology to enable acquisition of the ‘pure’ species spectrum.

This also demonstrates the extended spectral coverage (increase of ca. 200 cm<sup>-1</sup>) that is acquired with no loss in spectral resolution, due to the extended width of this new sensor type. The final goal is to obtain reliable real-time kinetic data on two phase reaction mixtures in which substrates in the organic phase undergo oxidation.

### Model reaction for development of the biphasic reaction monitoring protocol

The model reaction chosen for this study is the oxidation of styrene with a dinuclear manganese catalyst (Figure 1). Under biphasic conditions (styrene/water) 30% conversion to the epoxide was observed after 14 h (Figure 2) as determined by phase separation and <sup>1</sup>H NMR analysis of the organic phase.

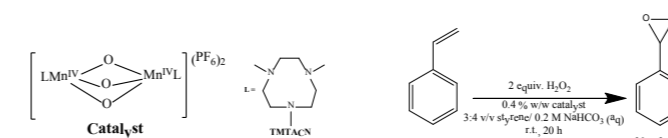


Figure 1: Oxidation of styrene in aqueous carbonate with H<sub>2</sub>O<sub>2</sub> catalysed by a manganese catalyst.

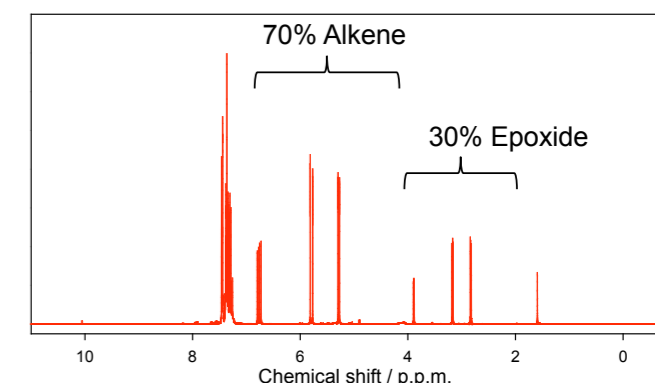


Figure 2: <sup>1</sup>H NMR spectrum of the organic phase (in CDCl<sub>3</sub>) after 14 h.

### System Design

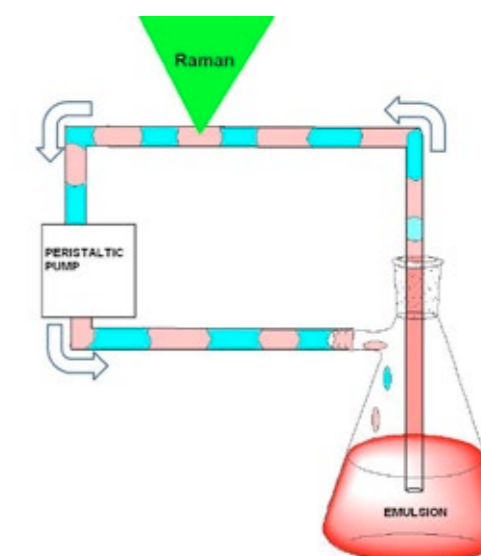


Figure 3: Schematic of the flow system / Raman sampling setup is shown above.

The biphasic mixture is emulsified in the reactor and a peristaltic pump connected with chemically resistant tubing (PTFE) samples the mixture continuously.

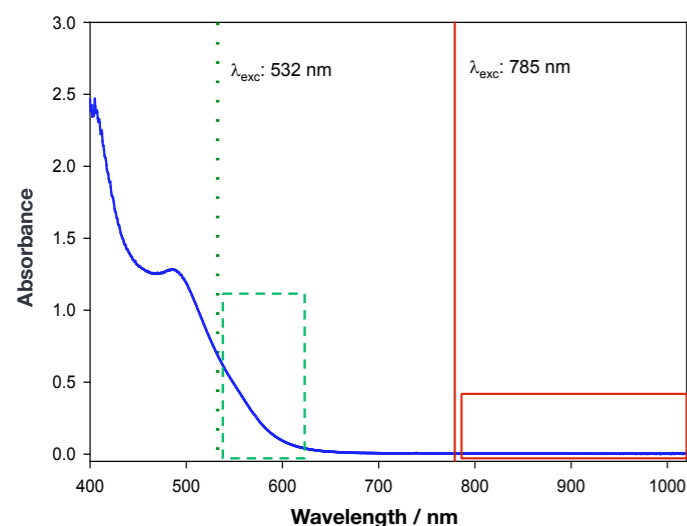


Figure 3: UV/vis absorption spectra of the catalyst (3 mM, blue line) in water, the inner filter effect is substantial at 532 nm (green) while there is no absorption at 785 nm (red).

Upon entering the PTFE tube, the emulsion breaks and a two phase (organic and aqueous) flow (slug flow, 10 mL/s) is obtained. The slug flow allows very short periods in which only either an aqueous, organic or air pocket is present within the confocal volume of the Raman probe.

The sample withdrawn must be returned to the reaction vessel with a minimum of delay and hence the flow rate and time available to record a spectrum of individual slugs is limited – this requires rapid, high sensitivity, detection.

### Wavelength choice and inner filter effects

Visible absorption by a catalyst in the aqueous phase limits collection of Raman scattering due to

reabsorption. Initially 785 nm is optimum; however, over the course of the reaction the absorbance decreases and hence to maximise for spectral range 532 nm was used also (Figure 3).

### Inline Raman

The experimental setup used is comprised of an iDus CCD Low Dark Current Deep-Depletion detector and Shamrock 163 spectrograph (Andor Technology), a 532 nm fibre coupled laser (200 mW at sample, Cobolt lasers) and Raman probe (Avantes). 1,000 Raman spectra were acquired in 60 s using 30 ms exposure time per acquisition, as shown in Figure 4 after discrimination.

Based on their chemical fingerprint features, the spectra obtained could be discriminated into four groups: organic and aqueous phase, aqueous phase only, organic phase only or gas bubbles. The spectra are sorted using a simple algorithm and spectra of solely organic and solely aqueous phases are retained.

The spectra showing only the organic and aqueous phase were extracted and, after normalization using the Raman bands of the PTFE tubing, the deviation (in percentage) of selected bands of the styrene (C=C stretch) and H<sub>2</sub>O<sub>2</sub> (O-O stretch) in each spectrum was plotted. For both the graphs the median (black line) and the mean value are within 2%.

Taking this approach the very large difference in absolute Raman intensity between the strongly scattering styrene and weakly scattering H<sub>2</sub>O<sub>2</sub> is not a factor in the analysis and hence high S/N spectra can be acquired from each phase every 60 s.

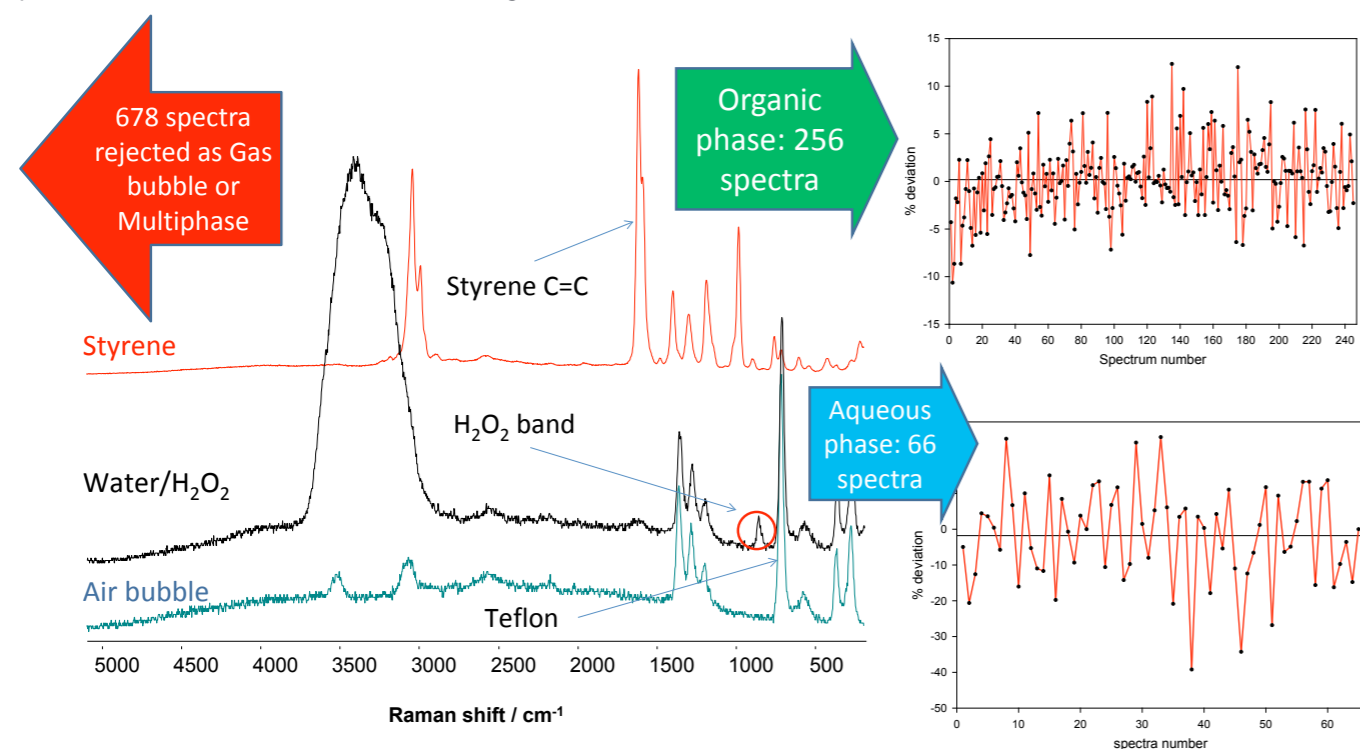


Figure 4: Spectrum of the organic (styrene) phase (red), of the aqueous phase (black) and where a bubble of air occupied the focal volume of the probe. These spectra were extracted from the 1,000 spectra obtained.

### Conclusions


The advantages and technical challenges facing the application of non-invasive Raman scattering in real-time reaction monitoring in biphasic solutions is demonstrated and a solution to the large intensity differences between components of interest is shown to be feasible.

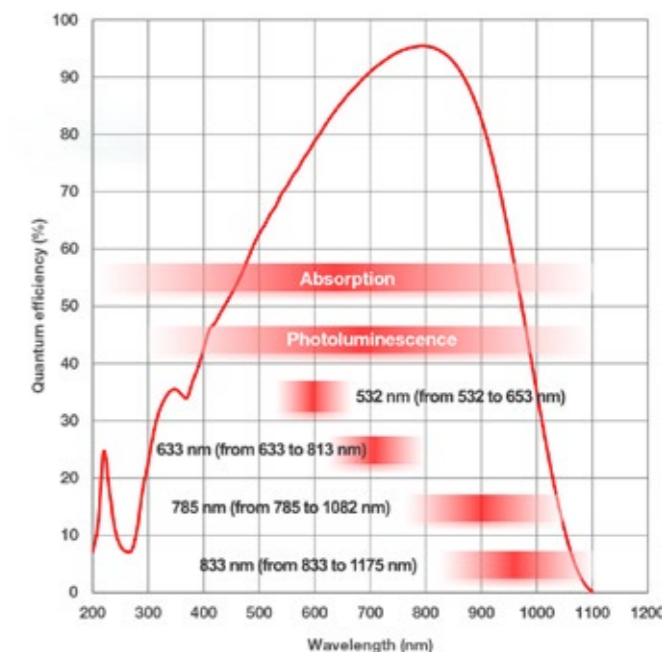
### References

- [1] B. Cornills, J. Mol. Catal. A-Chem, 143, 1 (1999)
- [2] S. Hardy, I. M. de Wispelaere, W. Leitner, M. A. Liauw, Analyst, 138, 819 (2013)
- [3] W. A. Shafer, S. Hobbs, J. Rehm, D. A. Rakestraw, C. Orella, M. McLaughlin, Z. Ge, C. J. Welch, Org. Process. Res. Dev., 11, 870 (2007)

### Learning more about Low-Dark Current Deep-Depletion (LDC-DD) CCD - maximizing signal to noise ratio in the NIR



- ✓ Peak QE up to 95% at 850 nm
- ✓ 10x lower dark noise than traditional back-illuminated deep-depletion technology
- ✓ Thermo-Electric cooling down to -95°C - negligible dark noise without the inconvenient use of liquid nitrogen cooling 
- ✓ Ultravac™ vacuum technology - maintains quantum efficiency performance year after year
- ✓ 2000 x 256 high CCD matrix
  - ✓ 15 μm pixel - high resolution spectroscopy
  - ✓ 30 mm sensor - superior simultaneous band-pass capture
- ✓ Fringe-suppression technology - low optical etaloning in the NIR
- ✓ USB connection



Quantum Efficiency curve for iDus 416 LDC-DD camera

### For more information ...



Search for our technical note entitled 'Low Dark Current Deep-Depletion (LDC-DD) Technology' at [andor.com/learning](http://andor.com/learning) or visit [andor.com/idus](http://andor.com/idus)

# Fibre Probe Based Raman Spectroscopy Biosensor for Surgical Robotics

Praveen Cheriyan Ashok  
School of Physics and Astronomy, St Andrews University, UK

In many surgical procedures involving the excision of tumorous tissue, the surgeon is challenged in deciding when the excision is complete whilst at the same time trying to minimize the amount of healthy tissue removed. This is particularly challenging during laparoscopy or keyhole surgery, and even more so if robotic surgery is included, where the view of the tissue and the tactile feedback are restricted, or absent. Researchers are turning to photonic techniques such as Raman spectroscopy, which can offer powerful detection capability in the field of bio-medical optics that aids in the identification of the chemical constituents of tissues and cells. This in turn can assist the surgeon in making a reliable diagnosis as regards the type of tissue. A group at the University of St Andrews [1,2] has tackled this problem by designing, building and demonstrating a robotic based analytical tool to assist surgeons in such surgical procedures.

## Introduction

Many surgical procedures are conducted nowadays with the assistance of robotic systems. Ashok et. al. [1] have developed a Raman probe based system to complement current standard diagnostic techniques such as histological examination. In their design a Raman probe based sensor was integrated into a surgical robot - ARAKNES (Array of Robots Augmenting the KiNematics of Endoluminal Surgery) [3], with the aim of demonstrating a tool for robot-assisted laparoscopic surgery. Laparoscopy is a type of surgical procedure that allows a surgeon to access the inside of the body with keyhole surgery, for example the abdomen, without having to make large incisions in the skin.

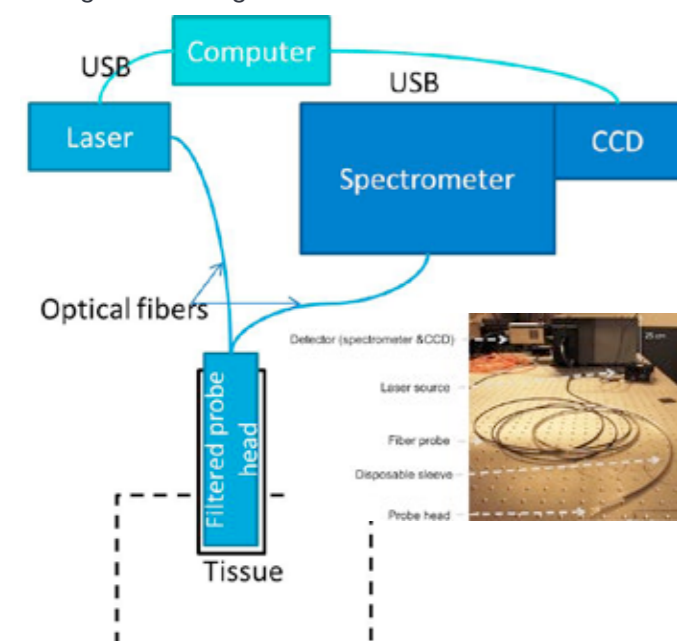


Figure 1: A schematic layout of the optical system showing the main components: a Newton CCD camera, Shamrock 303i spectrograph, the diode laser and the Raman probe (Emvision LLC), and probe head with disposable sleeve.

Raman spectroscopy can offer complementary information to, and possibly exceeding, purely vision and touch, regarding tissue morphology and chemical composition; this provides a basis for having multimodal information to aid decision making. The use of fiber based Raman probes has been demonstrated in various studies for in-vivo and ex-vivo tissue analysis [4] [5] [6]. Ashok and his co-workers show that such information can improve identification of the boundary or margin between healthy tissue and cancerous tissue during the surgical procedure [1,2].

## Setup

A schematic of the spectroscopy part of the system is shown in Figure 1. The Raman sensor consists of four principal subsystems:

- A laser diode operating at 785 nm (LuxxMaster, PD-LD) to excite the sample, with typical input power of 100 mW at the sample.
- A fiber-based Raman probe (Emvision LLC), with an excitation delivery fiber of 200  $\mu\text{m}$  core diameter, and a collection bundle of seven fibers each with 200  $\mu\text{m}$  core diameter.
- A spectrograph (Shamrock 303i) using an F-number matcher and incorporating a 400 l/mm grating, blazed at 850 nm to facilitate good collection efficiency.
- A CCD detector (Newton DU920P-BR-DD) that has a thermo-electrically (TE) cooled deep-depletion, back-illuminated sensor to ensure optimum sensitivity in the NIR region.

The fiber probe cables were 5 m long to allow for a safe working distance of the spectroscopy system from the operating table, and were terminated by two SMA connectors at the ends connected to the excitation



Figure 2: The fiber probe being held and manipulated by the robotic arm of ARAKNES.

laser and spectrograph. At the other end of the cable was a rigid probe head with length of 50 mm and diameter of 3.8 mm. It contained a low-pass filter at the excitation side and a long-pass filter at the collection side to reduce the background fluorescence from the optical fiber. A GRIN lens mounted at the tip of the probe head set the working distance from the end of the probe head to approximately 1 mm. The resulting size of the excitation beam at the sample was  $\sim 500 \mu\text{m}$  in diameter. A number of key features were designed into the probe head to ensure that:

- It could be manoeuvred easily by the robotic arm inside the abdominal cavity.
- The stiffness of the first 30 cm approximately of the fiber probe next to the head could be varied in such a way so as to aid the positioning of the probe head during the insertion and retraction phases of the surgical procedure.

A picture of the fiber probe being manipulated by the robot arm is shown in Figure 2.

A disposable sterile sleeve, into which the probe was inserted, was used to maintain sterility of the probe during the surgical procedure. A sapphire window was bonded to the end of the sleeve and this allowed optical access to the tissue from the probe head. The probe head was pushed up against the 1 mm thick sapphire window. Since the probe head had a working distance of 1 mm - the sleeve-head assembly was used in contact mode i.e. the sapphire window was brought into contact with the tissue when taking the Raman spectral data, thus minimizing any variability in the signal due to different sample-probe distances.

Another very important component of the system was the user-compatible software interface. Clearly the tool has to be user friendly to surgeons and medical staff, whose expertise is not analytical spectroscopy, but who want to know whether the tissue under test is healthy or cancerous. Ashok et. al. implemented a supervised multivariate classification algorithm to classify the different tissue types. Two key features incorporated

within their protocol for analyzing the data were:

- Adapting the configuration to avoid inter-patient variability in data.
- Ensuring the sensor system is generic for use in binary discrimination between any types of tissue i.e. that it is not restricted to a particular tissue type.

The interface that performs binary tissue classification was based on a machine learning algorithm, where a training dataset was obtained locally from the same patient going through the operation. The aim of the sensor is to assist the surgeon in identifying the separation line between two different tissue types, when such differentiation is otherwise visually ambiguous. Given the known presence of a tumor prior to excision, it will have two known tissue types (tumor, type-A, and non-tumor, type-B). Hence this gives the opportunity to train the binary classifier for the margin identification task by using sample areas from the two distinct tissue regions from the specific patient concerned. Having trained the system to identify the two different tissue types, it can then be used to identify the unknown tissue type in the regions around the boundary between healthy and cancerous tissue, and thereby allow the surgeon to determine the location of that boundary.

## Results and Discussion

In order to test the efficiency of the system, proof-of-principle tests were carried out on excised tissues that were visually similar. Adipose tissues derived from various animals were used in this tissue discrimination analysis. A typical Raman spectrum captured from Bovine adipose tissues is shown in Figure 3. With chemometric analysis of the subtle differences between spectral features from different samples the different tissue types can be identified. An accuracy of 95% was obtained in discriminating these tissue types.

The development of this system represents a significant step forward in the development of robotically assisted surgical tools incorporating on-line photonic based diagnostic techniques. Specifically Raman spectroscopy

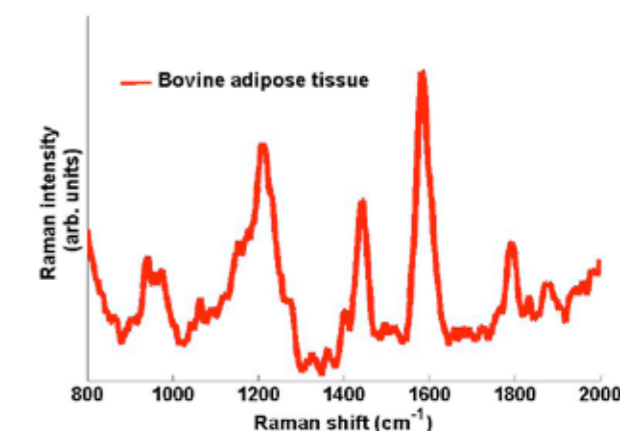


Figure 3: Typical Raman spectra taken from Bovine adipose tissue. The spectrum was captured with an exposure time of 1s.



can provide a wealth of complementary information for tissue discrimination and thereby aid surgeons in making more informed decisions whilst carrying out surgical procedures. The St Andrews group approach has been a modular one, which will allow such tools to be used in other platforms. They have developed a protocol which overcomes patient-to-patient variability, and binary discrimination capability that can be applied to a range of different tissue types.

### Acknowledgement

Appreciation is gratefully extended to Dr. Praveen Ashok for his assistance. Images courtesy of the group at the University of St. Andrews.


### References

- [1] P. C. Ashok, M. E. Giardini, K. Dholakia, and W. Sibbett, A Raman spectroscopy bio-sensor for tissue discrimination in surgical robotics. *J Biophotonics* (2013)
- [2] P. C. Ashok, N. Krstaji, M. E. Giardini, K. Dholakia, and W. Sibbett, Raman Spectroscopy Sensor for Surgical Robotics - Instrumentation and Tissue Differentiation Algorithm. *Biomedical Optics and 3-D Imaging*, (Optical Society of America, Miami, Florida), p. JM3A.26, (2012)
- [3] [www.araknes.org](http://www.araknes.org) ARAKNES Project (2008)
- [4] J. T. Motz, S. J. Gandhi, O. R. Scepanovic, A. S. Haka, J. R. Kramer, R. R. Dasari, and M. S. Feld, Real-time Raman system for in vivo disease diagnosis. *J. Biomed. Opt.* 10, (2005)
- [5] J. T. Motz, M. Hunter, L. H. Galindo, J. A. Gardecki, J. R. Kramer, R. R. Dasari, and M. S. Feld, Optical fiber probe for biomedical Raman spectroscopy. *Appl. Optics* 43, p542-554 (2004)
- [6] A. Mahadevan-Jansen, M. F. Mitchell, N. Ramanujam, U. Utzinger, and R. Richards-Kortum, Development of a Fiber Optic Probe to Measure NIR Raman Spectra of Cervical Tissue In Vivo. *Photochem. Photobiol.* 68, p427-431 (1998)

“ We chose the Andor analytical instruments due to the high sensitivity of the DU920P BR-DD CCD camera and the small form factor of the Shamrock 303i spectrometer.

While its performance is every bit as good as a bench-top system, the Shamrock's compact size and low weight lent it a degree of portability as well. This was important to us as we originally developed our Raman spectroscopy bio-sensor to be compatible with a surgical Robotic system. One of the design constraints for us was to develop a robust system which occupies relatively small space.

The Andor system we used offered both high performance and robustness. Also the software development kit helped us to develop an interface that could be easily integrated into the main interface of the surgical robot.



Dr. Praveen Cheriyan Ashok, Post-doctoral fellow in the optical manipulation group of University of St. Andrews, Scotland.

”

### Find out more ...



Search for the webinar entitled 'Optofluidic Raman Spectroscopy' at [andor.com/learning](http://andor.com/learning)



## Diffuse Reflectance Spectroscopy and Fluorescence Spectroscopy as techniques for identification of lung cancers

JW. Spliethoff *et al.*

Antoni van Leeuwenhoek Hospital, Netherlands

Tissue biopsies are used to ensure accurate diagnosis of cancerous tissue of the lungs and the treatment planning that follows thereafter. However, a significant number of transthoracic biopsies to analyse lung lesions give indeterminate results. A group working at the Antoni van Leeuwenhoek hospital in the Netherlands are tackling this problem with the use of biophotonic techniques<sup>[1]</sup> – namely Diffuse Reflectance Spectroscopy (DRS) and Fluorescence Spectroscopy (FS) – to assess how the accuracy of the diagnostic procedure may be improved. Spliethoff *et al.*<sup>[1,2]</sup> reporting in the journal *Lung Cancer* outline their design and testing of prototype instrumentation for the addition of these photonic based modalities to the standard histopathology technique, and demonstrate their benefit to the final diagnosis.

### Introduction

A lung needle biopsy is a procedure where the radiologist removes a small piece of lung tissue for examination using a long narrow bore extraction needle which is inserted into the chest cavity (thorax) and directed to the tissue lesion to be investigated<sup>[3]</sup>. The guidance of the needle tip to the correct site is achieved with real-time computed tomography (CT) imaging. When the biopsy is done through the wall of the chest it is called a transthoracic lung biopsy, or a transthoracic needle biopsy (TNB). The excised tissue is then analysed by the radiologist using the gold standard technique of histopathology, where slices of the tissue are stained with standard hematoxylin/eosin (H&E) techniques to bring out the contrast in the different components of the tissue.

The motivation of Spliethoff and his coworkers was to evaluate if optical spectroscopy incorporated at the tip of the biopsy needle can, in real-time, facilitate improved accuracy in the diagnosis of lung biopsies. This added modality for collection of information could help address the relatively high level (circa 23%) of reported failure rates for this type of biopsy<sup>[4]</sup>.

### Experimental Setup

A portable spectroscopy system was set up to carry out ex-vivo diffuse reflectance spectroscopy (DRS) and fluorescence spectroscopy (FS) on freshly excised tissue from lung lesions extracted from a range of patients diagnosed with the disease. A schematic layout of the optical system is shown in Figure 1. The system contained two spectrographs (2x Shamrock SR163) and two detectors, one for the visible to near-infrared (NIR) region covering 400 to 1100 nm (Andor iDus DU420A-BRDD) and the other to cover the NIR region from 900 to 1700 nm (Andor iDus DU492A-1.7). An optical fiber probe consisting of four optical fibers was used to deliver the light to the sample from the light sources and to collect the DRS and FS signals for delivery to the spectrometers. There were two light sources used, a broadband (360 - 2500 nm) Tungsten halogen lamp for the DRS measurements and a diode laser (wavelength at 377 nm) for excitation of the autofluorescence species within the tissue in the FS measurements. An individual optical fiber coupled each light source to the sample, and individual fibers coupled the measurable signal to each of the spectrometers. The end of the fiber probe system for sampling the tissue was placed a short distance from the tissue to be tested – typically less than 2 mm.

For integration, control of the system and acquisition of data, a custom-made LabView program was developed (National Instruments). Measurements were made at multiple points within each sample. With the two spectrograph - two detectors combination it was possible to capture DRS spectral data over the whole range from 400 nm to 1600 nm. The FS data was captured in the 400 to 800 nm region with the deep-depletion back-illuminated (DU420A-BRDD) detector only. After the optical measurements were complete the samples were put through the histopathology process

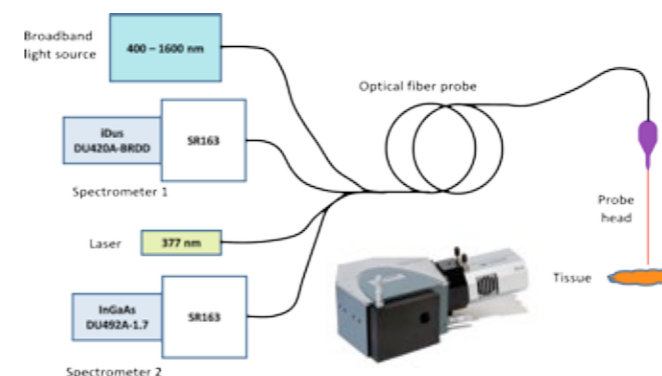


Figure 1: A schematic diagram of the main components of the optical system.

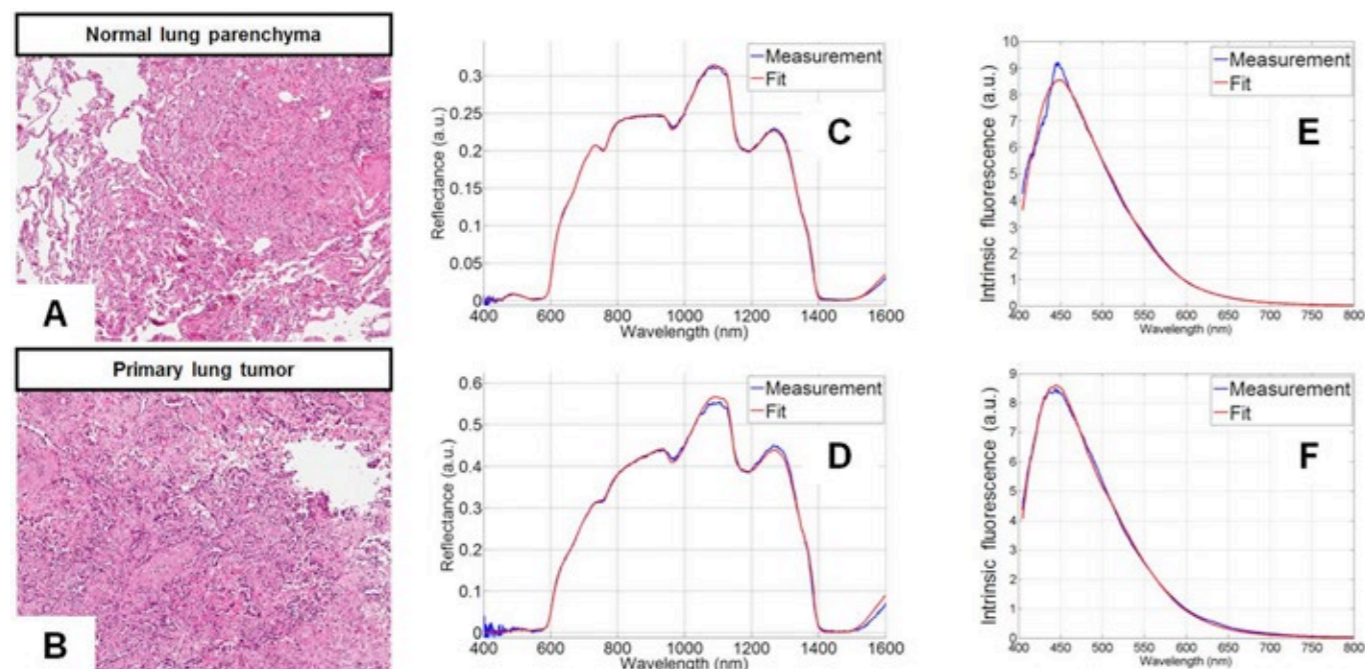


Figure 2: Typical DRS and FS spectra including fitted spectra from the models for both healthy and cancerous tissue. On the left are shown typical images of stained tissue samples used in histopathology. Figure reproduced with permission from journal Lung Cancer, 80 (2013).

and classified by the pathologist without any knowledge of the results from the optical data.

Typical DRS spectra from healthy and cancerous tissue are shown in figures 2(C) and 2(D) respectively. The main spectral features of interest are influenced by the absorption in the visible range (400 - 800 nm) associated with the chromophores of oxygenated and deoxygenated haemoglobin of normal tissue, and the main absorbers in the NIR range (900 - 1600 nm) of water, collagen and fat. When diffuse scattering is considered it is dominated by Mie and Rayleigh (elastic) scatter. Mie scattering occurs when light interacts with particles of a size comparable to the wavelength of the light, whilst Rayleigh scatter occurs when the light interacts with particles much smaller than the wavelength of incident light. The main characterizing parameters derived from the scatter were:

- the reduced scattering at 800 nm, and,
- the comparison of the Mie scattering to the total scattering from the tissue.

The total scatter was considered to principally consist of both Mie and Rayleigh scattered light.

Taking into account parameters such as the absorption coefficient, the reduced scattering coefficient and the distances from the exit facets of the probe fibers and the sample tissue, a proven DRS analytical model [5] was used to fit spectra to the measured DRS spectra. Fits to the typical DRS spectra are included in figures 2(C) and 2(D).

Similarly an FS analytical model was constructed for analysis of the captured fluorescence spectra. The FS spectra were first corrected for scattering and absorption. Using the intrinsic fluorescence spectra

(with excitation of 377 nm) for collagen, elastin, FAD and NADH, the corrected spectra were fitted by the deduced spectra from the model. Typical FS spectra for healthy and tumorous tissue are shown in figures 2(E) and 2(F) respectively and corresponding fits derived from the FS analytical model are also included. The FS results proved particularly useful in distinguishing between necrotic and non-necrotic tissue. Necrotic tissue consists of dead or dying cells in a localized region brought about by factors external to the cells, such as infection, toxins, or trauma.

A measure of the cellular metabolic state can be provided by what is called the optical reduction-oxidation (redox) ratio. Spliethoff et. al. defined this as the ratio of NADH to NADH+FAD. NADH stands for hydrogenated nicotinamide adenine dinucleotide and is a macromolecule found in all living cells; chemically it can act as a reducing agent. FAD stands for flavin adenine dinucleotide and likewise is a macromolecule found in all living cells. Both these chemicals perform vital roles in the underlying metabolic processes of the cell.

Using a classification and regression trees (CART) algorithm with the derived parameters (tissue composition, physiological characteristics and metabolic activity) from the spectral data, Spliethoff et.al. were able to classify the different tissue types. Comparing with the gold standard of histopathology allowed a specificity and sensitivity to be determined for the classification achieved using their optical technique.

Discrimination between lung parenchyma and tumor tissue using all the DRS data achieved a sensitivity of 98% and a specificity of 86%. Using the FS parameters they achieved discrimination between necrotic and non-necrotic tissue with 91% sensitivity and 91% specificity.

The group's work clearly demonstrated that DRS spectroscopy can offer accurate real-time diagnosis of malignant lung tissue, and it further showed how FS spectroscopy can be used to identify necrotic tissue. This highlights the potential that optical techniques may offer in the future for enhancement of the diagnostic quality of various biopsy procedures.

### Acknowledgments

Figure 2 is reproduced with permission from the journal Lung Cancer, 80, (2013).

### References

- [1] Spliethoff JW, Evers DJ, Klomp HM, van Sandick JW, Wouters MW, Nachabe R, Lucassen GW, Hendriks BHW, Wesseling J, Ruers TJM, Improved identification of peripheral lung tumors by using diffuse reflectance and fluorescence spectroscopy. Lung Cancer, 80, p165- 171 (2013)
- [2] Supplementary data associated with paper above can be found at <http://dx.doi.org/10.1016/j.lungcan>.
- [3] [www.youtube.com/watch%3Fv%3DabvYaB2Vcml](http://www.youtube.com/watch%3Fv%3DabvYaB2Vcml), [www.nlm.nih.gov/medlineplus/ency/article/003860.htm](http://www.nlm.nih.gov/medlineplus/ency/article/003860.htm)
- [4] Priola A, Priola S, Diagnostic accuracy and complication rate of CT-guided fine needle aspiration biopsy of lung lesions: a study based on the experience of the cytopathologist. Acta Radiology, 51, p527-33 (2010)
- [5] Farrell TJ, Patterson MS, Wilson B, A diffusion theory model of spatially resolved, steady-state diffuse reflectance for the non-invasive determination of tissue optical properties in vivo. Medical Physics, 19, p879-88 (1992)

### Find out more ...



Search for the application note 'Diffuse Reflectance Spectroscopy and Fluorescence Spectroscopy' at [andor.com/learning](http://andor.com/learning)

### Learning more about 'Diffuse Reflectance Spectroscopy' use in clinical diagnosis

Diffuse Reflectance Spectroscopy is an increasing popular technique for non-invasive clinical diagnostics, with clinical instrumentation already being at very advanced development stage.

A team at the Cancer Diagnostic Research Division, Shizuoka Cancer Center Research Institute in Shizuoka, Japan, developed a hyperspectral imaging instrument for rapid *in situ* and non-invasive identification and discrimination of malignant melanoma and other types of skin lesions. The aim of the research is to provide a systematic and reliable tool to determine whether an (invasive) biopsy is absolutely necessary to confirm the malignant nature of a skin lesion. Reducing the number of unnecessary biopsies based on visual and subjective inspection has important implications in terms of patient comfort and cost.

The system detection system focusing on 'visible' wavelengths consisted of an ultrasensitive Andor iXon EMCCD DU897E-BV detector and an Inspector V8E hyperspectral spectrograph (Specim, Finland).

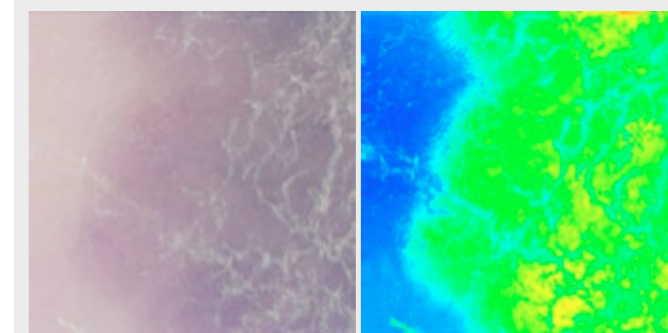


Figure 3: A standard dermoscopy image of a skin lesion (melanoma) is shown on the left and the derived hyperspectral image is shown on the right.



Search for the application note 'Hyperspectral Imaging for Clinical Diagnosis' at [andor.com/learning](http://andor.com/learning)

# Optical Etaloning in CCDs and EMCCDs

## Technical Note

In the field of modern scientific-grade Charge Coupled Devices (CCDs) detectors the arrival of back-illuminated CCDs and Electron-Multiplying Charge Coupled Devices (EMCCDs) has offered key enabling technology for the growing range of applications where the photon signal available is extremely low. Such applications include low-light cell microscopy and fast chemical mapping. This document presents one of the key challenges associated with the use of back-illuminated, CCDs for Near-Infrared (NIR) detection, namely optical etaloning, and outlines with particular reference to a manufacturing process called ‘fringe suppression’.

### Introduction

The ability of a CCD camera to capture photons and ‘detect’ the associated ‘photoelectrons’ that are generated is typically measured in terms of signal-to-noise ratio (SNR). The SNR can be expressed as follows:

$$SNR = \frac{QE \cdot P}{\sqrt{\left(\frac{N_{RN}}{G}\right)^2 + F^2(N_{DN}^2 + N_{CIC}^2 + N_{SN}^2)}} \quad [1]$$

Where **QE** (Quantum Efficiency) is the probability of an incoming photon being absorbed in the photosensitive region of the sensor,  $N_{RN}$  the readout noise of the sensor,  $N_{DN}$  its dark noise,  $N_{CIC}$  the noise associated with clocking induced charge (CIC) and  $N_{SN}$  the shot noise associated with the incoming photon signal [1]. **P** denotes the photon flux of the signal incident on the pixel, **G** is the gain or multiplication factor should an EMCCD be used, and **F** denotes the Noise Factor. The noise factor takes into account the fact that in the case where Gain is applied to a raw signal to amplify it, the input noise to the amplification stage is also amplified.

It is clear that achieving high **SNR** depends not only on careful minimization of the different sensor noise sources (cooling for the dark noise, slower readout speed and/or use of electron multiplying gain for the readout noise, fast vertical clocking for CIC), but also on high sensor QE.

### Back-illumination of CCDs – the attraction of high Quantum Efficiency in the Visible and NIR Regions

The QE of a CCD is governed by its ability to absorb incoming photons in the photosensitive silicon also known as the depletion region. It is only in this region that photons are converted into electron-hole pairs,

which are then confined by means of electric fields into a ‘pixel’. The charges held in these pixels can then be read out.

Shorter wavelength photons (blue light) are absorbed closer to the silicon surface, while longer wavelength photons can travel deeper into the silicon matrix before being absorbed. Photons with wavelength above 1.1  $\mu\text{m}$  do not have enough energy to create an electron-hole pair and so cannot be detected: a silicon CCD is effectively transparent at these longer wavelengths.

Figure 1 shows the absorption depth of photons as a function of wavelength in crystalline silicon.

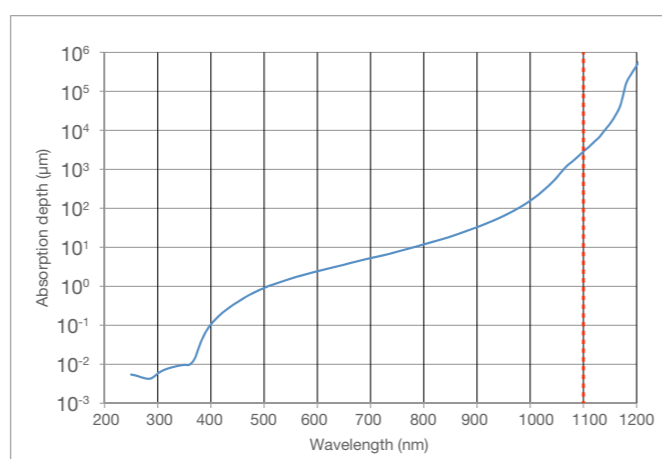


Figure 1: Absorption depth in Silicon at 300K as a function of incident photon wavelength[1]

In front-illuminated CCDs, incoming photons must first transverse a polysilicon electrode structure and a silicon oxide (SiO) insulating layer (see Figure 2). The electrode structure can absorb and reflect part of the incoming photon flux before it reaches the photosensitive region. This region is also referred to as the depletion region (it is depleted in mobile charge carriers) and has the ability to capture and store the electrons generated from the photon signal.

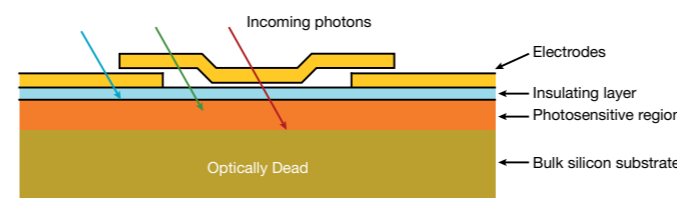


Figure 2: Typical front-illuminated CCD (cross section)

This absorption in the surface layers is extremely pronounced in the ultraviolet (<350 nm), resulting in near zero detection for UV photons. This design structure also limits the QE of front illuminated devices to ~50% in the visible.

In order to eliminate the losses incurred at the front surface, a back-illuminated (BI) configuration can be adopted. The back-illumination process involves the removal of the bulk silicon substrate by mechanical grinding and chemical etching, allowing direct exposure of the active photosensitive region to the incoming photons as shown on Figure 3. These devices can exhibit peak QE's of up to 95% with appropriate anti-reflection (AR) coatings. NIR QE of standard back-illuminated CCDs can be further enhanced by the use of a thicker photosensitive region, also referred to as the **deep depletion** region. Material with higher resistivity is used in these devices.

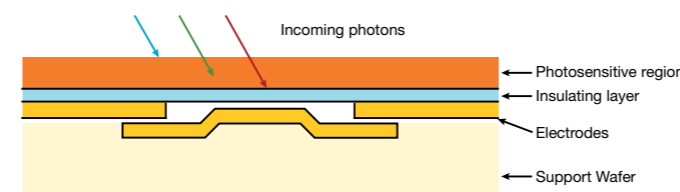


Figure 3: Typical back-illuminated CCD (cross section)

- The thicker photosensitive region offers a greater absorption path to longer wavelength photons, and subsequently lowers the probability for these photons

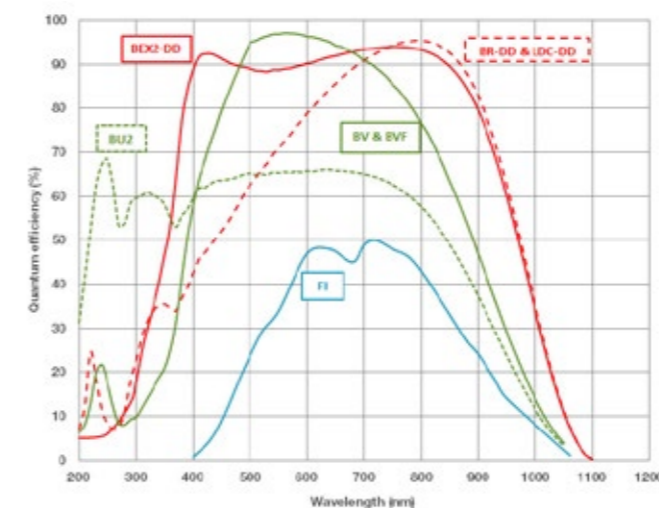


Figure 4: Typical QE performance at +25°C of front-illuminated (‘FI’), back-illuminated visible-optimized (‘BV’), UV-enhanced back-illuminated (‘BU2’), back-illuminated deep-depletion CCDs with NIR AR-coating (‘BR-DD’) and broadband dual AR-coating (‘BEX2-DD’). The new BI Low Dark Current Deep-Depletion (‘LDC-DD’) [4] and ‘BR-DD’ have identical QE characteristics.

transversing the whole way across the active region (refer to Figure 1).

- The higher resistivity material allows the electric fields, created by applying voltages to the electrodes, to penetrate the entire depth of the now thicker photosensitive region and hence better collect and confine photoelectrons within the pixels.

These devices are known as back-illuminated, deep-depletion (BI-DD) CCDs.

A property of back-illuminated CCDs that is often overlooked is their propensity to generate constructive and destructive optical interference when illuminated with coherent photons. This behavior is especially pronounced in the NIR and can lead to signal modulation as high as 40%. This highly undesirable effect can be extremely disruptive for applications based on NIR Raman, NIR photoluminescence or Bose Einstein Condensate (BEC) studies.

Front-illuminated CCDs however, do not suffer from optical etaloning. In these devices, incoming photons with longer absorption lengths (longer wavelengths) do not encounter any interface with highly mismatched refractive indexes after reaching the photosensitive region. These photons have therefore a very low chance of being reflected back-and-forth in the depletion region and create interferences. Photons that are not absorbed in this region are lost in the optically dead bulk silicon substrate.

The following section describes the origin of the interferometer behavior of back-illuminated CCDs, by comparing their structure with a particular type of interferometer called a Fabry-Pérot étalon.

The ultra-thin cavity formed by the depletion region, with parallel and highly reflective surfaces is akin to a Fabry-Pérot étalon configuration.

### Back-illuminated CCDs and analogy to the Fabry-Pérot étalon

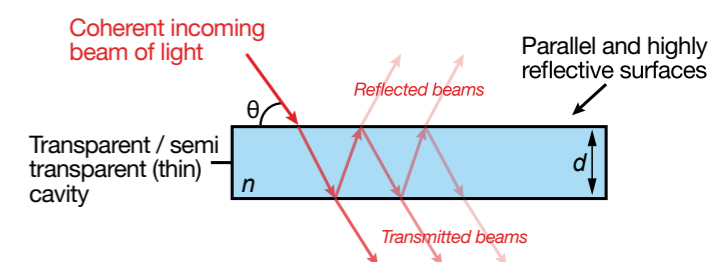


Figure 5: Typical Fabry-Pérot étalon configuration

A typical Fabry-Pérot étalon consists of a thin, transparent optical medium with two flat, parallel and highly reflective surfaces. A back-illuminated CCD is akin to this configuration, with the depletion region sandwiched between a silicon oxide insulating layer and air / vacuum with highly mismatched refractive indexes

which create highly reflective interfaces. Coherent light entering the cavity can undergo multiple reflections, which can lead to the generation of destructive and constructive interference, largely determined by the Etalon configuration in terms of its thickness or 'optical length', and the dielectric properties of the material within it. This is illustrated in Figure 7.

The modulation characteristics of the signal are governed by the following equation (adapted from [3]):

$$T = \left[ \frac{1}{1 + \left(\frac{2F}{\pi}\right)^2 \sin^2\left(\frac{\varphi}{2}\right)} \right] \quad \text{[ii]}$$

$$\text{with } F \approx \frac{n\sqrt{R}}{(1-R)} \text{ and } \varphi = \frac{2\pi}{\lambda} 2nd \cos\theta \quad \text{[iii]}$$

where **T** is the transmittivity function of the étalon, **F** is a measure of the quality of the étalon known as Finesse, **R** is the reflectivity of the étalon surfaces (assumed to be identical for simplification), **φ** the roundtrip phase change of the photon signal, **n** the refractive index of the cavity medium, **d** the distance between the étalon surfaces and **θ** the angle of the incoming light relative to the étalon surface. Figure 6 shows the influence of the cavity Finesse on the quality of the étalon.

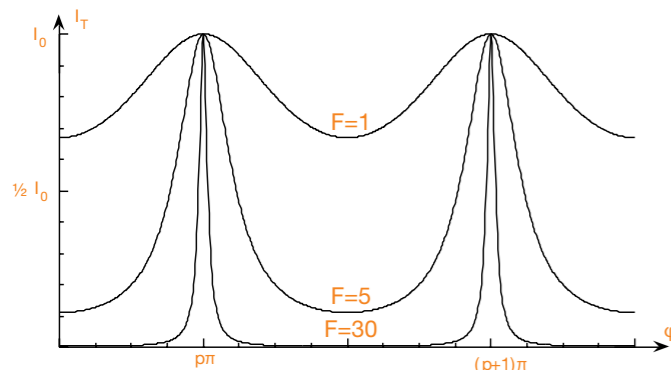


Figure 6: Influence of cavity Finesse on fringing sharpness and amplitude (integers p and p+1 refer to consecutive fringes separated by one roundtrip through the cavity)

Etalons with highly reflective surfaces (high R, hence high Finesse) show sharper transmission peaks, while etalons with less reflective surfaces (low R, hence low Finesse) lead to increasingly smeared fringes.

The spacing in wavelength between two successive transmitted optical intensity maxima of a Fabry-Pérot étalon is given by the **free spectral range (FSR)**. Typical FSR values for back-illuminated CCDs are shown below:

- Back-illuminated visible-optimized CCDs: FSR is ~5 - 10 nm for photons in the 700 - 1100 nm region,
- Back-illuminated deep-depletion CCDs: FSR is ~2 - 4 nm for photons in the 700 - 1100 nm region

### Spectral and spatial etaloning in back-illuminated CCDs

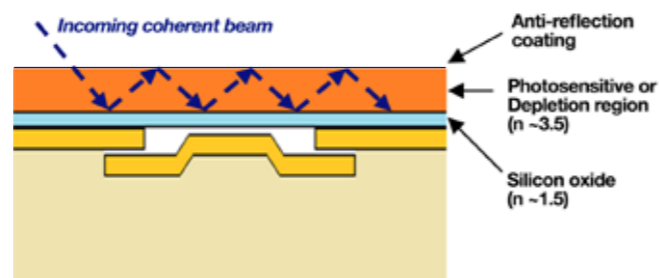


Figure 7: Back-illuminated, sensor and étalon cavity structure analogy (n refers to the refractive index)

The thickness of the depletion region in back-illuminated CCDs can typically vary between 10-50 μm (type-dependent). The absorption length of NIR photons in silicon can be several times this thickness (see Figure 1), which effectively means that the CCD is semi-transparent at these wavelengths. The CCD depletion region has a refractive index of ~3.5, while the silicon oxide (insulating) layer has a refractive index of ~1.5. This significant mismatch means that this interface is extremely reflective, so that NIR photons entering the depletion region and reaching the insulating layer without being absorbed will be reflected back towards the front surface of the depletion region. These reflected photons can in turn reach the front surface of the active region. This front surface is typically AR-coated in order to minimize the refractive index mismatch at the silicon-air interface. This increases the transmission of photons through this interface and consequently limits further potential internal reflections in the active silicon region.

However since AR coatings are not perfect, longer wavelength photons can undergo several reflections back-and-forth in the depletion region, and under conditions dictated by the cavity characteristics create destructive and constructive interferences. These multiple reflections increase the chance of NIR photons being absorbed and therefore increase the QE of the sensor in the NIR. The interference pattern linked to the wavelength-selectivity of the étalon is referred to as **spectral fringing**. Since the surfaces of the depletion region are not perfectly parallel or flat, local variations of a few μm of the depletion region thickness can change

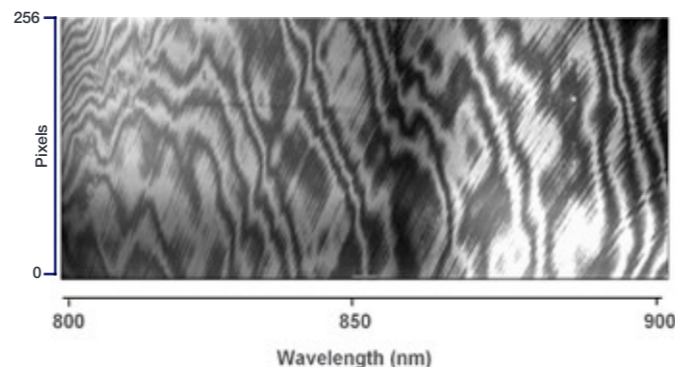


Figure 8: Un-binned image of a broadband tungsten lamp taken with a Shamrock 750 spectrograph and a back-illuminated visible-optimized iDus 420A-BV

the interference conditions and alter the spectral fringing pattern. This effect is referred to as **spatial fringing**. The detected fringing pattern on a CCD is a combination of both spectral and spatial contributions. The combined effects of spectral and spatial fringing is illustrated in Figure 8 back-illuminated sensor (BV) optimized for the visible region.

For spectroscopy applications, multiple wavelengths are dispersed across the CCD sensor width: the subsequent fringing pattern superimposed on the 'normal' signal will show the contribution of each interfering wavelength. The AR coatings applied to the front surface of the depletion region are specific to a particular wavelength range. Outside the range of greatest efficiency, the Finesse of the cavity is affected, resulting in a gradual decrease of fringe sharpness and intensity. Note: single NIR coatings applied to back-illuminated, deep depletion CCDs are typically optimized at around 800 nm, bringing the peak QE to ~95% at this wavelength.

### Influence of cooling temperature

Cooling is used to minimize thermally generated 'dark noise' contribution in CCDs in order to maximise SNR. The latest generation of thermo-electric (TE) based scientific cameras can achieve sensor temperatures down to -100°C.

Cooling also has an influence on the photon absorption depth in crystalline silicon, changing the refractive index of the active region [2], while also inducing small mechanical changes in the active silicon structure. This means that the étalon characteristics also change with temperature, resulting in temperature-dependent constructive and destructive interference patterns as illustrated on Figure 9.

Maintaining a stable cooling temperature is therefore strongly recommended when dealing with relative or absolute intensity data correction, where such changes

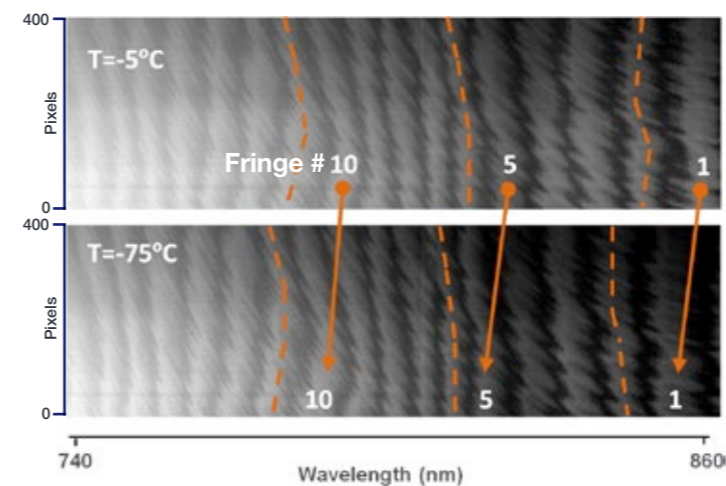


Figure 9: Un-binned images of broadband tungsten source captured with a back-illuminated visible-enhanced Newton DU971-BV EMCCD at different sensor cooling temperatures. Camera was coupled to a Shamrock 750 spectrograph. Fringes are identified by a number to facilitate visualization of the shift with temperature.

in the sensor characteristics and interference pattern will have an impact on the baseline data taken with the standard calibration source.

### Minimizing etaloning in back-illuminated CCDs

Interference patterns in back-illuminated CCDs can never be totally suppressed, but can be reduced through a range of techniques highlighted here.

Front-illuminated CCDs do not suffer from optical etaloning. In these devices, incoming photons with longer absorption lengths (longer wavelengths) do not encounter any interface with highly mismatched refractive indexes after reaching the photosensitive region. These photons therefore have a very low chance of being reflected back-and-forth in the depletion region and create interferences. Photons that are not absorbed in this region are lost in the optically dead bulk silicon substrate.

Several approaches can be used to minimize etaloning in the NIR for back-illuminated CCDs:

- **Increase of the depletion region thickness** - this increases the probability for NIR photons being absorbed in the photosensitive region before being able to undergo multiple reflections and a loss in coherence due to the longer optical pathlengths.
- **Relative / absolute intensity calibration** - the use of a stable reference lamp with known emissivity characteristics can be used to correct for the optical response of a CCD camera, or the optical transfer function of an optical instrument (e.g. spectrograph, CCD cameras and light coupling optics). The term Radiometric calibration is typically used to describe an absolute spectral calibration.
- **Extensive binning to increase interference pattern averaging (spectroscopy)** - by increasing the dispersion of the signal in the 'spatial' axis (vertically) on a back-illuminated CCD coupled to the output of a spectrograph, extensive vertical binning can be used (e.g. 'full vertical binning' mode). This creates a better chance to efficiently average the signal intensity modulation linked to the alternation of constructive (peaks) and destructive (dips) interference fringes imaged across the CCD pixel columns.
- **'Fringe-suppression' process** - this refers to a CCD manufacturing process consisting of the controlled 'roughening' of the back surface of the depletion region, hence disrupting the interferometer cavity parallelism. This helps reduce the coherence within the interfering light signal.

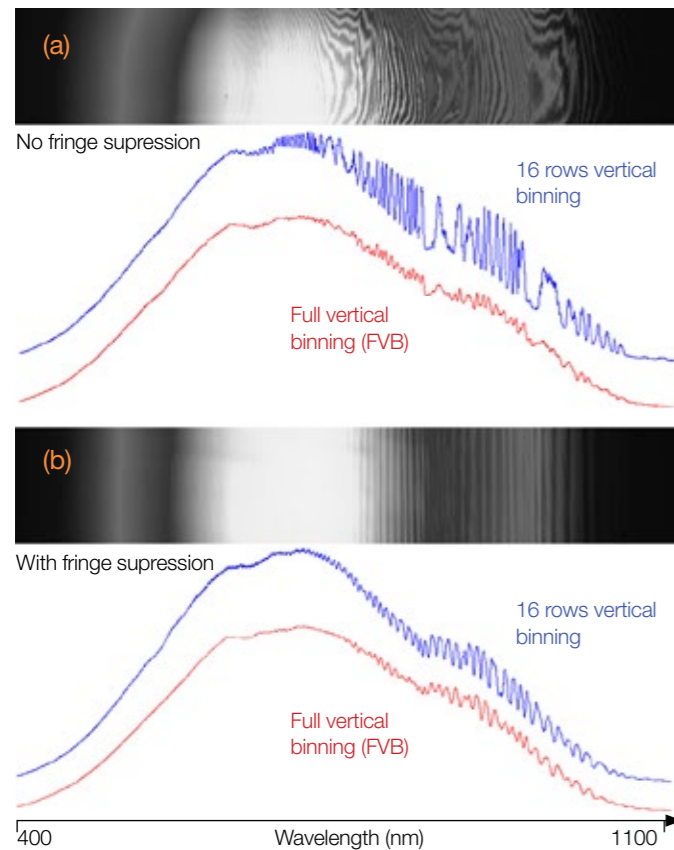


Figure 10: FVB spectra (red) and 16-row high binned track spectra (blue) of a broadband tungsten source acquired with a ‘standard’ back-illuminated CCD (a), and a back-illuminated CCD with ‘fringe-suppression’ (b) attached to a Shamrock 750 spectrograph. Corresponding un-binned images are shown above each dataset.

All of these methods are sensitive to the way light is coupled onto the CCD and to the sensor temperature.

Table 1 highlights the effectiveness of the fringe suppression process for different types of back-illuminated CCDs. It should be noted that this process intrinsically can have large variations within it.

	BI Deep-Depletion without fringe suppression	BI Deep-Depletion with fringe suppression	BI visible-enhanced without fringe suppression	BI visible-enhanced with fringe-suppression
Peak modulation in the NIR	> 10%	1-5%	20-40%	10-20%

Table 1: Typical (peak - peak) signal modulation for a range of back-illuminated CCD types.

### Influence of vertical binning

The modulation amplitude will also depend on the number of pixels binned on the sensor. Figure 10 shows a number of binned continuous broadband spectra in 2 binning configurations: (i) Full Vertically Binning (FVB) on a 3.2 mm high sensor, and (ii) a 16-row high binned track in the middle of the same sensor. Spectral profiles are for (a) a ‘standard’ back-illuminated CCD without fringe suppression (BV) and, (b) a back-illuminated with fringe suppression (BVF): both sensors are optimized for the visible region.

The following observations can be made:

- FVB spectra show little difference in terms of etaloning modulation for either ‘standard’ or ‘fringe-suppression’ CCD types. This can be explained by the effective averaging of the interference fringe modulation over a large number of rows on the CCD.
- In the case of ‘Imaging Spectroscopy’ (multi-track spectroscopy, hyperspectral imaging or superfast spectral acquisition modes such as Crop Mode), a limited number of CCD rows are binned at one time. The averaging of the fringe modulation is not as effective, as clearly shown on Figure 9 (16 rows vertically binned spectra). In this case the ‘fringe-suppression’ technology is clearly of great benefit, showing two to three times less modulation amplitude than the ‘standard’ back-illuminated CCD type.

### Back-illuminated deep-depletion CCDs – High NIR QE and Low etaloning

BI-DD sensors boast typical peak QE up to 95% in the NIR (see Figure 4), which makes these devices the platform of choice for low light NIR detection. But the other great advantage of such sensors is the extremely low etaloning exhibited in the NIR.

The thicker photosensitive region of BI-DD sensors offers a greater absorption path for longer wavelength photons, which minimizes the chance for multiple reflections of NIR photons occurring inside the étalon-like photosensitive region structure. This consequently greatly reduces the detected signal modulation in the NIR. In order to further reduce this signal modulation, sensor manufacturers apply a ‘Fringe-suppression’ process described in previous section.

Figure 11 illustrate the signal modulation in BI-DD CCDs. It clearly shows the much reduced fringing pattern on both image and vertically binned spectra compared to thinner back-illuminated CCDs (see Figure 10).

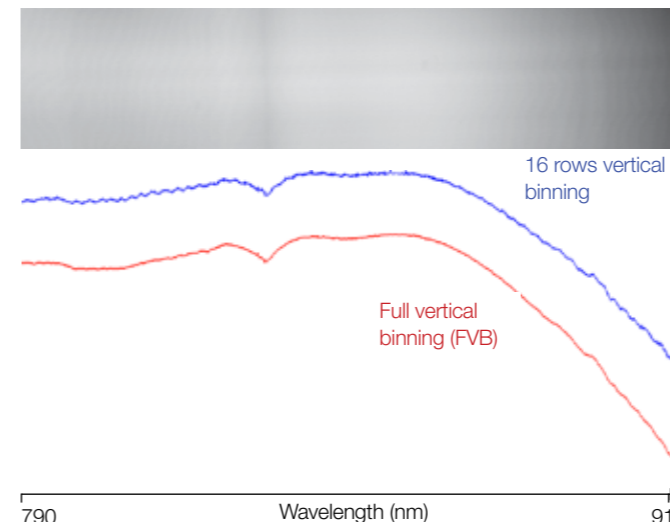


Figure 11: FVB spectra (red) and 16 rows high binned track spectra (blue) of a broadband tungsten source acquired with a back-illuminated deep-depletion CCD attached to a Shamrock 750 spectrograph.

### Summary

- Optical etaloning in the NIR is an issue on any back-illuminated back-thinned CCD
- Signal modulation can be up to 40%
- Optical etaloning in the NIR is not an issue on Front-illuminated CCDs
- Optical etaloning on any back-illuminated CCD can only be minimized, never completely removed
- ‘Fringe-suppression’ technology is an effective way to reduce etaloning effects in both back-thinned CCDs optimized for the visible and deep-depletion CCDs optimized for the NIR region.
- BI-DD CCDs exhibit greatly reduced optical etaloning compared to thinner back-illuminated CCDs.

### Appendix A

Key spectroscopy sensors and platforms by Andor

Andor sensor code	Description	Wavelength range (nm)	Peak QE	Fringe suppression process	Peak modulation amplitude	Dark current	Andor platform
FI	Front-illuminated	400 - 1100	58% @ 770 nm	Not necessary	0%	Very low	iDus 401, Newton 940, NewtonEM 970, NewtonEM 971
OE	Open electrode	<200 – 1100	58% @ 770 nm	Not necessary	0%	Very low	iDus 420, Newton 920
BV	Back-illuminated, Visible-optimized AR coating	<200 – 1100	97% @ 550 nm	No	20-40% (850 – 900 nm)	Low	iDus 420, Newton 920, Newton 940, NewtonEM 970, NewtonEM 971
BVF	Back-illuminated, Visible-optimized AR coating	<200 – 1100	97% @ 550 nm	Yes	10-20% (850 – 900 nm)	Low	iDus 401, iDus 420, Newton 920, NewtonEM 970
BR-DD	Back-illuminated, deep-depletion NIR-optimized AR coating	<200 – 1100	95% @ 800 nm	Yes	1-5% (~ 950 nm)	High	iDus 420, Newton 920
BEX2-DD	Back-illuminated, deep-depletion Broadband, dual AR coating	300 – 1100	93% @ 800 nm 92% @ 420 nm	Yes	1-5% (~ 950 nm)	High	iDus 420, Newton 920
LDC-DD	Back-illuminated, deep-depletion NIR-optimized AR coating	<200 – 1100	95% @ 800 nm	Yes	1-5% (~ 950 nm)	Low	iDus 416

Table 2: Summary of main front-illuminated and back-illuminated, back-thinned sensors offered by Andor

### References

- Sensitivity of CCD cameras – some key factors to consider. <http://www.andor.com/learning-academy/sensitivity-of-ccd-cameras-key-factors-to-consider>
- Green, M.A. and Keevers, M. Optical properties of intrinsic silicon at 300 K. Progress in Photovoltaics, p.189-92, vol.3, no.3 (1995)
- G. Hernandez, Fabry-Pérot interferometers, Cambridge Studies in Modern Optics, Cambridge University Press, ISBN 0-521-32238-3 (1986)
- Low Dark Current Deep-Depletion (LDC-DD) Technology. [http://www.andor.com/learning-academy/low-dark-current-deep-depletion-\(lcc-dd\)-technology-a-new-standard-for-low-light-nir-spectroscopy](http://www.andor.com/learning-academy/low-dark-current-deep-depletion-(lcc-dd)-technology-a-new-standard-for-low-light-nir-spectroscopy)

# User Publications

<b>Prototype instrument development for non-destructive detection of pesticide residue in apple surface using Raman technology</b> , Sagar Dhakal <i>et al.</i> , Journal of Food Engineering 123, p94-103, doi:10.1016/j.jfoodeng.2013.09.025 (2014)	Newton 920P-BR-DD CCD
<b>Metal-coordination: using one of nature's tricks to control soft material mechanics</b> , Niels Holten-Andersen <i>et al.</i> , J. Mater. Chem. B, doi: 10.1039/C3TB21374A (2014)	iDus DU401A-BR-DD CCD
<b>Photophysical Properties of the Excited States of Bacteriochlorophyll f in Solvents and in Chlorosomes</b> , Dariusz M. Niedzwiedzki <i>et al.</i> , J. Phys. Chem. B, doi: 10.1021/jp409495m (2014)	iStar DH720-18H-13 ICCD
<b>A combined Raman-fluorescence spectroscopic probe for tissue diagnostics applications</b> , Riccardo Cicchi <i>et al.</i> , Proc. SPIE 8798, Clinical and Biomedical Spectroscopy and Imaging III, doi:10.1117/12.2031370 (2013)	iDus 420A-BR-DD CCD
<b>Anatomical variability of in vivo Raman spectra of normal oral cavity and its effect on oral tissue classification</b> , H. Krishna <i>et al.</i> , Biomedical Spectroscopy and Imaging 2(3), doi: 10.3233/BSI-130042 (2013)	iDus DU420A-BR-DD CCD, Shamrock 303i spectrograph
<b>Effect of the laser and light-emitting diode (LED) phototherapy on midpalatal suture bone formation after rapid maxilla expansion: a Raman spectroscopy analysis</b> , C. B. Rosa <i>et al.</i> , Lasers Med. Sci., doi: 10.1007/s10103-013-1284-7 (2013)	iDus 401A-BR-DD CCD, Shamrock 303i spectrograph
<b>Method for Assessing the Reliability of Molecular Diagnostics Based on Multiplexed SERS-Coded Nanoparticles</b> , Leigh SY <i>et al.</i> PLoS ONE 8(4): e62084, doi:10.1371/journal.pone.0062084 (2013)	Newton 920P-BR-DD CCD
<b>Monitoring angiogenesis using a human compatible calibration for broadband near-infrared spectroscopy</b> , R. Yang <i>et al.</i> , J. Biomed. Opt. 18(1), 016011, doi:10.1117/1.JBO.18.1.016011 (2013)	iDus 420A-BR-DD CCD, Shamrock 303i spectrograph
<b>Optofluidic Raman sensor for simultaneous detection of the toxicity and quality of alcoholic beverages</b> , P. C. Ashok <i>et al.</i> , J. Raman Spectrosc., 44: 795–797, doi: 10.1002/jrs.4301 (2013)	Newton 920P-BR-DD CCD, Shamrock 303i spectrograph
<b>Raman spectroscopy and imaging to detect contaminants for food safety applications</b> , K. Chao <i>et al.</i> , Proc. SPIE 8721, Sensing for Agriculture and Food Quality and Safety V, doi:10.1117/12.2018616 (2013)	Newton 920P-BR-DD CCD, Raman Explorer 785 spectrograph
<b>Single-nanoparticle detection and spectroscopy in cells using a hyperspectral darkfield imaging technique</b> , N. Fairbairn <i>et al.</i> , Proc. SPIE 8595: Colloidal Nanocrystals for Biomedical Applications VIII., doi:10.1117/12.981941 (2013)	Luca R EMCCD (and AOTF)
<b>The influence of surface properties on the plasma dynamics in radio-frequency driven oxygen plasmas: Measurements and simulations</b> , A. Greb <i>et al.</i> , Appl. Phys. Lett. 103, 244101, doi: 10.1063/1.4841675 (2013)	iStar DH334T-18U-C3 ICCD, Shamrock 500I-B1 spectrograph
<b>Validating in vivo Raman spectroscopy of bone in human subjects</b> , F. W. L. Esmonde-White, Proc. SPIE 8565, Photonic Therapeutics and Diagnostics IX, doi:10.1117/12.2005679 (2013)	Newton 920P-BR-DD CCD, HoloSpec f/1.8i spectrograph
<b>Rational Assembly of Optoplasmonic Hetero-nanoparticle Arrays with Tunable Photonic-Plasmonic Resonances</b> , Y. Hong <i>et al.</i> , Adv. Funct. Mater., doi: 10.1002/adfm.201301837 (2013)	iDus DU401A-BR-DD CCD, Shamrock 303i spectrograph
<b>Target-specific nanoparticles containing a broad band emissive NIR dye for the sensitive detection and characterization of tumor development</b> , T. Behnke <i>et al.</i> , Biomaterials 34(1), doi: 10.1016/j.biomaterials.2012.09.028 (2013)	iDus DU420A-BR-DD CCD, Shamrock 303i spectrograph
<b>Three-pulse multiplex coherent anti-Stokes/Stokes Raman scattering (CARS/CSRS) microspectroscopy using a white-light laser source</b> , K. Bito <i>et al.</i> , Chemical Physics 419:156-162, doi: 10.1016/j.chemphys.2013.02.007 (2013)	Newton DU920N-BR-DD CCD

<b>Tuning the 3D plasmon field of nanohole arrays</b> , M. Couture, Nanoscale 5, 12399-12408, doi: 10.1039/C3NR04002J (2013)	iDus DU401A-BR-DD CCD
<b>Wrapping and dispersion of multiwalled carbon nanotubes improves electrical conductivity of protein-nanotube composite biomaterials</b> , C. M. Vogue <i>et al.</i> , J Biomed Mater Res Part A 2013:101A:231–238 (2013)	iDus DU401A-BR-DD CCD, HoloSpec f/1.8i spectrograph
<b>Photo-induced oxidation of [FeII(N4Py)CH3CN] and related complexes</b> , A. Draksharapu <i>et al.</i> , Dalton Trans. 41, 13180-13190, doi: 10.1039/C2DT30392B (2012)	iDus InGaAs DU490A-1.7, Shamrock SR-163 spectrograph, iDus DV420A-BU2, Shamrock 303i
<b>Photoluminescence microscopy and spectroscopy of individualized and aggregated single-wall carbon nanotubes</b> , F. Schöppler <i>et al.</i> , Chemical Physics 413, p112–115, doi: 10.1016/j.chemphys.2012.08.011 (2012)	Newton DU920N-BR-DD CCD
<b>Propagation Lengths and Group Velocities of Plasmons in Chemically Synthesized Gold and Silver Nanowires</b> , B. Wild <i>et al.</i> , ACS Nano, 6 (1), p472–482, doi: 10.1021/nn203802e (2012)	Newton DU920N-BR-DD CCD, Shamrock 303i spectrograph
<b>Shifted excitation Raman difference spectroscopy at multiple wavelengths for in-situ meat species differentiation</b> , K. Sowoidnich <i>et al.</i> , Applied Physics B 108(4), p975-982, doi: 10.1007/s00340-012-5160-0 (2012)	iDus DU420A-BR-DD CCD
<b>Transcutaneous monitoring of steroid-induced osteoporosis with Raman spectroscopy</b> , J. R. Maher <i>et al.</i> , Proc. SPIE 8219, Biomedical Vibrational Spectroscopy V: Advances in Research and Industry, doi:10.1117/12.908361 (2012)	iDus DU420A-BR-DD CCD, HoloSpec f/1.8i spectrograph
<b>Integrated system for combined Raman spectroscopy-spectral domain optical coherence tomography</b> , Chetan A. Patil <i>et al.</i> , J. Biomed. Opt. 16(1), doi:10.1117/1.3520132 (2011)	Newton 920-BR-DD CCD, HoloSpec f/1.8i spectrograph
<b>Detection of Microcalcification in Tissue by Raman Spectroscopy</b> , Omer Tzang <i>et al.</i> , 2(3), Cardiovascular Engineering and Technology, p228-233, doi: 10.1007/s13239-011-0051-9 (2011)	iDus 401A-BR-DD CCD, Shamrock 303i spectrograph







## Customer Support

Andor products are regularly used in critical applications and we can provide a variety of customer support services to maximise the return on your investment and ensure that your product continues to operate at its optimum performance.

Andor has customer support teams located across North America, Asia and Europe, allowing us to provide local technical assistance and advice. Requests for support can be made at any time by contacting our technical support team at [andor.com/support](http://andor.com/support).

Andor offers a variety of support under the following format:

- On-site product specialists can assist you with the installation and commissioning of your chosen product
- Training services can be provided on-site or remotely via the Internet
- A testing service to confirm the integrity and optimize the performance of existing equipment in the field is also available on request.

A range of extended warranty packages are available for Andor products giving you the flexibility to choose one appropriate for your needs. These warranties allow you to obtain additional levels of service and include both on-site and remote support options, and may be purchased on a multi-year basis allowing users to fix their support costs over the operating life cycle of the products.



### Head Office

7 Millennium Way  
Springvale Business Park  
Belfast BT12 7AL  
Northern Ireland  
Tel: +44 (0)28 9023 7126  
Fax: +44 (0)28 9031 0792

### North America

425 Sullivan Avenue  
Suite 3  
South Windsor, CT 06074  
USA  
Tel: +1 860-290-9211  
Fax: +1 860-290-9566

### Japan

4F TK Sarugakucho Building  
2-7-6 Sarugaku-Cho  
Chiyoda-Ku  
Tokyo 101-0064  
Japan  
Tel: +81 (0)3-3518-6488  
Fax: +81 (0)3-3518-6489

### China

Room 1213, Building B  
Luo Ke Time Square  
No. 103 Huizhongli  
Chaoyang District  
Beijing 100101  
China  
Tel: +86 (0)10-5129-4977  
Fax: +86 (0)10-6445-5401

### Find us on

